Rotordynamic Forces Due to Annular Leakage Flows in Shrouded Centrifugal Pumps

Thesis by

Joseph Michael Sivo

In Partial Fulfillment of the Requirements
for the Degree of
Doctor of Philosophy

California Institute of Technology
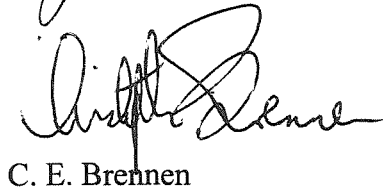Pasadena, California

1997

(Defended May 31, 1996)

Forward

At this juncture, the members of Mr. Sivo's graduate counseling committee, as well as his doctoral examination committee, would like to explain that Mr. Sivo's graduate study at the Institute was interrupted by six quarters of medical leave. During his periods of active study, he worked on several topics, some of which are complete works that have been published in refereed journals and conference proceedings. He has also carried out additional work — experimental, analytical, and computational in nature — that, while essentially complete, have not been put in final publication form. The Examination Committee believes that Mr. Sivo's already published work is amply sufficient to satisfy the thesis requirement of the Degree of Doctor of Philosophy. Accordingly, we have assembled these papers as the body of the thesis. The first three papers deal with the materials of the thesis title. The last chapter is concerned with a separate subject, supersonic film cooling. This work was supervised by Professor M. L. Hunt. It is our understanding from Professor Hunt and Professor Zukoski that Mr. Sivo was responsible for the experiment design of this work, an essential part of the research, which led eventually to the doctoral thesis of another student. All of the chapters are self-contained.
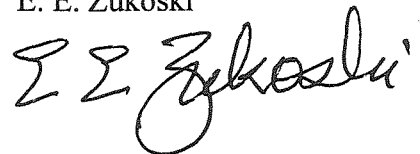
Examination Committee:

A. J. Acosta

T. Colonius

C. E. Brennen

E. E. Zukoski

T. K. Caughey

ROTORDYNAMIC FORCES DUE TO ANNULAR LEAKAGE FLOWS IN SHROUDED CENTRIFUGAL PUMPS

Joseph M. Sivo

Division of Engineering and Applied Science
California Institute of Technology
Pasadena, California

ABSTRACT

Previous experimental and analytical results have shown that discharge-to-suction leakage flows in the annulus of a shrouded centrifugal pump contribute substantially to the fluid induced rotordynamic forces (Adkins, 1988). Experiments conducted in the Rotor Force Test Facility (RFTF) at Caltech on an impeller undergoing a prescribed circular whirl have indicated that the leakage flow contribution to the normal and tangential forces can be as much as 70% and 30% of the total, respectively (Jery, 1986). Recent experiments at Caltech have examined the rotordynamic consequences of leakage flows and have shown that the rotordynamic forces are functions not only of the whirl ratio but also of the leakage flow rate and the impeller shroud to pump housing clearance. The forces were found to be inversely proportional to the clearance and a region of forward subsynchronous whirl was found for which the average tangential force was destabilizing. This region decreased with flow coefficient (Guinzburg, 1992).

The present research is a continuation of the previous experimental work and has been motivated by the rotordynamic stability problems with the recently developed Alternate Turbopump Design (ATD) of the Space Shuttle High Pressure

Oxygen Turbopump. The present study investigates the influence of swirl brakes, installed in the annular leakage path, as a means of reducing the undesirable rotordynamic forces over a range of flow rates. Also, the present study evaluates the effect on the rotordynamic forces of tip leakage restrictions at discharge used by the ATD for establishing axial thrust balance. As a first step to understanding the flow field in the leakage annulus, the region is probed with a laser velocimeter to provide basic information on these unsteady turbulent three-dimensional leakage flows and to serve as a standard of comparison for approximate theoretical models as well as applications of computational fluid dynamics.

Contents

Chapter 1

The Influence of Swirl Brakes on the Rotordynamic Forces
Generated by Discharge-to-Suction Leakage Flows
in Centrifugal Pumps

THE INFLUENCE OF SWIRL BRAKES ON THE ROTORDYNAMIC FORCES GENERATED BY DISCHARGE-TO-SUCTION LEAKAGE FLOWS IN CENTRIFUGAL PUMPS

Joseph M. Sivo, Allan J. Acosta,
Christopher E. Brennen, and Thomas K. Caughey
Department of Mechanical Engineering
California Institute of Technology
Pasadena, California

ABSTRACT

Increasing interest has been given to swirl brakes as a means of reducing destabilizing rotordynamic forces due to leakage flows in new high speed rocket turbopumps. Although swirl brakes have been used successfully in practice (such as with the Space Shuttle HPOTP), no experimental tests until now have been performed to demonstrate their beneficial effect over a range of leakage flow rates. The present study investigates the effect of swirl brakes on rotordynamic forces generated by discharge-to-suction leakage flows in the annulus of shrouded centrifugal pumps over a range of subsynchronous whirl ratios and various leakage flow rates. In addition, the effectiveness of swirl brakes in the presence of leakage inlet (pump discharge) swirl is also demonstrated. The experimental data demonstrates that with the addition of swirl brakes a significant reduction in the destabilizing tangential force for lower flow rates is achieved. At higher flow rates, the brakes are detrimental. In the presence of leakage inlet swirl, brakes were effective over all leakage flow rates tested in reducing the range of whirl frequency ratio for which the tangential force is destabilizing.

NOMENCLATURE

$[A^*]$	Rotordynamic force matrix
B	Depth of logarithmic spiral channel on swirl vane
c	Cross-coupled damping coefficient, normalized by $\rho\pi\omega^2 R_2^2 L\varepsilon$
C	Direct damping coefficient, normalized by $\rho\pi\omega^2 R_2^2 L\varepsilon$
$F^*_x(t)$	Lateral horizontal force in the laboratory frame
$F^*_y(t)$	Lateral vertical force in the laboratory frame
F^*_{ox}	Steady horizontal force
F^*_{oy}	Steady vertical force
F^*_n	Force normal to whirl orbit
F_n	Force normal to whirl orbit normalized by $\rho\pi\omega^2 R_2^2 L\varepsilon$
F^*_t	Force tangent to whirl orbit
F_t	Force tangent to whirl orbit normalized by $\rho\pi\omega^2 R_2^2 L\varepsilon$
F_1, F_2	Lateral forces in rotating frame
H	Clearance between impeller shroud and housing
k	Cross-coupled stiffness coefficient normalized by $\rho\pi\omega^2 R_2^2 L\varepsilon$
K	Direct stiffness coefficient normalized by $\rho\pi\omega^2 R_2^2 L\varepsilon$
L	Axial length of impeller
M	Direct added mass coefficient normalized by $\rho\pi\omega^2 R_2^2 L\varepsilon$
Q	Volumetric leakage flow rate
R_2	Radius of impeller at leakage inlet
u_s	Mean leakage inlet path velocity of fluid
u_θ	Mean leakage inlet swirl velocity of fluid

$x^*(t)$ Horizontal displacement of impeller on its orbit

$y^*(t)$ Vertical displacement of impeller on its orbit

α Turning angle of logarithmic spiral channel on swirl vane

Γ Leakage inlet swirl ratio, $u_\theta/\omega R_2$

ε Eccentricity of impeller's circular whirl orbit

ρ Density of leakage fluid

ϕ Leakage flow coefficient, $u_s/\omega R_2$

ω Main shaft radian frequency

Ω Whirl radian frequency

INTRODUCTION

Previous experimental and analytical results have shown that discharge-to-suction leakage flows in the annulus of a shrouded centrifugal pump contribute substantially to the fluid induced rotordynamic forces (Adkins, 1988). Experiments conducted in the Rotor Force Test Facility (RFTF) at Caltech on an impeller undergoing a prescribed whirl have indicated that the leakage flow contribution to the normal and tangential forces can be as much as 70% and 30% of the total, respectively (Jery, 1986). Recent experiments at Caltech have examined the rotordynamic consequences of leakage flows and have shown that the rotordynamic forces are functions not only of the whirl ratio but also of the leakage flow rate and the impeller shroud to pump housing clearance. The forces were found to be inversely proportional to the clearance and a region of *forward subsynchronous whirl was found for which the average tangential force was destabilizing. This region decreased with flow coefficient (Guinzburg, 1992a).

The motivation for the present research is that the previous experiments have shown that leakage inlet (pump discharge) swirl can increase the cross-coupled stiffness coefficient (in some tests by over 100%) and hence increase the range of positive whirl for which the tangential force is destabilizing. One might therefore surmise that if the swirl velocity within the leakage path were reduced, then the destabilizing tangential force might be reduced. One way of reducing the leakage flow swirl is with the use of ribs or swirl brakes on the housing. In fact, swirl brakes installed upstream of the interstage seal on the Space Shuttle Main Engine High Pressure Oxygen Turbopump completely eliminated the subsynchronous whirl motion over the steady state operating range of the unit (Childs, 1990). The present study investigates the influence of swirl brakes on the rotordynamic forces generated by discharge-to-

suction leakage flows in shrouded centrifugal pumps over a range of subsynchronous whirl ratios and various leakage flow rates typical of present rocket turbopump designs. In addition, the effectiveness of swirl brakes in the presence of leakage inlet (pump discharge) swirl is also demonstrated.

ROTORDYNAMIC FORCES

Figure (1) shows a schematic of the hydrodynamic forces that act on a rotating impeller whirling in a circular orbit. F^*_x and F^*_y are the instantaneous lateral forces in the laboratory frame. Ω is the whirl radian frequency and ω is the main shaft radian frequency. The eccentricity of the orbit is given by ε. The lateral forces are given in linear form as:

$$\begin{pmatrix} F^*_x(t) \\ F^*_y(t) \end{pmatrix} = \begin{pmatrix} F^*_{ox} \\ F^*_{oy} \end{pmatrix} + [A^*] \begin{pmatrix} x^*(t) \\ y^*(t) \end{pmatrix} \qquad (1)$$

F^*_{ox} and F^*_{oy} are the steady forces which result from flow asymmetries in the volute. $[A^*]$ is the rotordynamic force matrix. It is a function of the mean flow conditions, pump geometry, whirl frequency ratio Ω/ω and if outside the linear range it may also be a function of the eccentricity ε. In the case of a circular whirl orbit:

$$x^*(t) = \varepsilon cos(\Omega t) \qquad (2)$$

$$y^*(t) = \varepsilon sin(\Omega t) \qquad (3)$$

The normal and tangential forces for a circular whirl orbit are given by (Jery, 1986 and Franz 1989):

$$F^*_n(t) = \frac{1}{2}(A^*_{xx} + A^*_{yy})\varepsilon \qquad (4)$$

$$F^*_t(t) = \frac{1}{2}(-A^*_{xy} + A^*_{yx})\varepsilon \qquad (5)$$

ROTORDYNAMIC COEFFICIENTS AND STABILITY

To study the stability of an impeller, it is convenient for rotordynamicists to fit the dimensionless normal force F_n to a quadratic function of the whirl ratio and to fit the dimensionless tangential force F_t to a linear function of the whirl ratio. The expressions are given by:

$$F_n = M\left(\frac{\Omega}{\omega}\right)^2 - c\left(\frac{\Omega}{\omega}\right) - K \qquad (6)$$

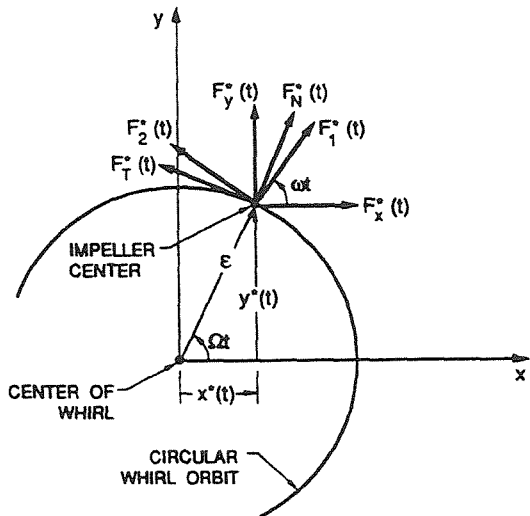$$F_t = -C\left(\frac{\Omega}{\omega}\right) + k \qquad (7)$$

FIGURE 1. SCHEMATIC OF THE FLUID-INDUCED FORCES ACTING ON AN IMPELLER WHIRLING IN A CIRCULAR ORBIT.

FIGURE 2. LEAKAGE FLOW TEST SECTION (ZHUANG, 1989).

where the dimensionless coefficients are the direct added mass (M), direct damping (C), cross-coupled damping (c), direct stiffness (K), and cross-coupled stiffness (k). As can be seen from equation (7), a positive cross-coupled stiffness is destabilizing because it starts the forward whirl of the impeller since it is equal to the tangential force at zero whirl ratio. Also, from equation (6), a large negative direct stiffness is destabilizing because it promotes a positive normal force which increases the eccentricity of the whirl orbit.

A convenient measure of the rotordynamic stability is the ratio of the cross-coupled stiffness to the direct damping (i.e. k/C) termed the whirl ratio. This is just a measure of the range of positive whirl frequency ratios for which the tangential force is destabilizing.

TEST APPARATUS

The present experiments were conducted in the Rotor Force Test Facility (RFTF) at Caltech. The leakage flow test section of the facility is shown in Figure (2).

The working fluid is water. The main components of the test section apparatus consist of a solid or dummy impeller (or rotating shroud), a housing (or stationary shroud) instrumented for pressure measurements, a rotating dynamometer (or internal force balance), an eccentric whirl mechanism (not shown), a leakage exit seal ring and a leakage inlet swirl vane (shown installed in Figure (3)). The solid impeller is used so that leakage
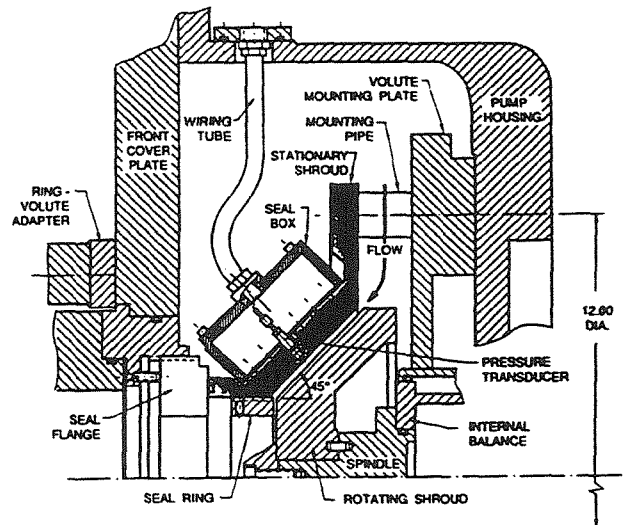
flow contributions to the forces are measured but the main through flow contributions are not experienced. The inner surface of the housing has been modified to accommodate meridional ribs or swirl brakes along the entire length of the leakage annulus. The ribs are each 3/16 of an inch wide and 2 mm high. Up to 8 equally spaced ribs can be installed. The leakage flow annulus between the impeller and housing is inclined at 45° to the axis of ratation. The nominal clearance between the solid impeller and the housing can be varied by axial adjustment of the housing. The flow through the leakage path is generated by an auxiliary pump. The solid impeller is mounted on a spindel attached to the rotating dynamometer connected to a data acquisition system which permits measurements of the rotordynamic force matrix. Jery, 1986 and Franz, 1989 describe the operation of the dynamometer. The eccentric drive mechanism imposes a circular whirl orbit on the basic main shaft rotation. The radius of the circular whirl orbit (or eccentricity) can be varied. The seal ring at the leakage exit models a wear ring. The clearance between the seal ring and impeller face is adjustable. The effect of swirl was investigated by installing a swirl vane at the leakage inlet to introduce pre-rotated fluid in the direction of shaft rotation. Figure (3) shows that the vane consists of a logarithmic spiral channel with a turning angle of 2°. The swirl ratio Γ (the ratio of the leakage flow circumferential velocity to the impeller tip velocity) is varied by changing the leakage flow rate. The
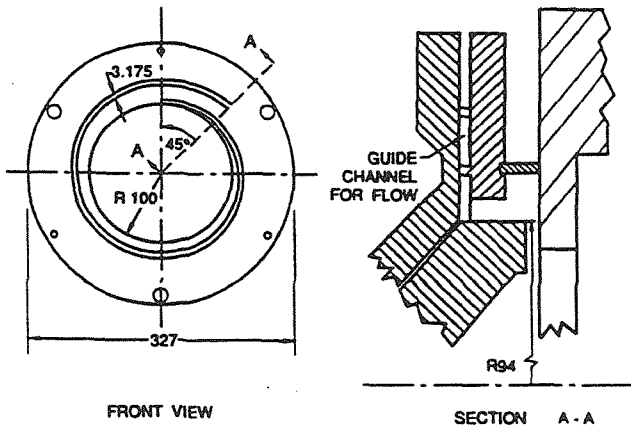
For the 2000 RPM runs, tests are performed for whirl frequency ratios in the range $-0.6 \leq \frac{\Omega}{\omega} \leq +0.7$ at 0.1 increments. Tests with the swirl vane installed are conducted at a shaft speed of 2000 RPM and the same flow rates as above. With the swirl vane, the above leakage flow rates yield swirl ratios Γ of 0.0, 0.5, 1.0 and 1.5, respectively. The above test matrix is summarized in Tables 1 and 2.

FIGURE 3. INSTALLATION OF LEAKAGE INLET SWIRL VANE. DIMENSIONS IN MM (GUINZBURG, 1992b).

swirl ratio depends on the flow coefficient according to:

$$\frac{\Gamma}{\phi} = \frac{H}{B\, Tan(\alpha)} \qquad (8)$$

B is the depth of the logarithmic spiral channel equal to 0.125 in. A derivation of equation (8) can be found in Guinzburg, 1992a.

TEST MATRIX

This experiment is designed to measure the rotordynamic forces due to simulated leakage flows for different parameters such as whirl frequency ratio, shaft speed, leakage flow coefficient, number of swirl brake ribs and leakage inlet swirl ratio. For all tests a nominal annulus clearance H of 0.167 in, a whirl eccentricity ε of 0.0465 in and a leakage exit face seal clearance of 0.04 in were maintained. Tests without leakage inlet swirl were conducted at shaft speeds ω of 1000 and 2000 RPM, leakage flow rates Q of 0, 10, 20 and 30 GPM and 0, 4 and 8 brake ribs. For the 1000 RPM runs, the above flow rates correspond to flow coefficients ϕ of 0.0, 0.026, 0.052 and 0.077, respectively. For the 2000 RPM runs, the above flow rates correspond to flow coefficients ϕ of 0.0, 0.013, 0.026 and 0.039, repectively. The above flow coefficients cover the range of typical leakage rates for the new Space Shuttle Alternate Turbopump (ATP) presently being developed. For the 1000 RPM runs, tests are performed for whirl frequency ratios in the range $-0.9 \leq \frac{\Omega}{\omega} \leq +0.9$ at 0.1 increments.

TABLE 1. TESTS WITHOUT SWIRL

RPM	Ω/ω	Brakes	Q (GPM)	ϕ
1000	−0.9 to +0.9	0	0	0.0
			10	0.026
			20	0.052
			30	0.077
		4	0	0.0
			10	0.026
			20	0.052
			30	0.077
		8	0	0.0
			10	0.026
			20	0.052
			30	0.077
2000	−0.6 to +0.7	0	0	0.0
			10	0.013
			20	0.026
			30	0.039
		4	0	0.0
			10	0.013
			20	0.026
			30	0.039
		8	0	0.0
			10	0.013
			20	0.026
			30	0.039

TABLE 2. TESTS WITH SWIRL

RPM	Ω/ω	Brakes	Q (GPM)	ϕ	Γ
2000	−0.6 to +0.7	0	0	0.0	0.0
			10	0.013	0.5
			20	0.026	1.0
			30	0.039	1.5
		4	0	0.0	0.0
			10	0.013	0.5
			20	0.026	1.0
			30	0.039	1.5
		8	0	0.0	0.0
			10	0.013	0.5
			20	0.026	1.0

RESULTS FOR TESTS WITHOUT LEAKAGE INLET SWIRL

Figures (4) and (5) show plots of the dimensionless rotordynamic coefficients for 2000 and 1000 RPM, respectively for the three different number of brake ribs. Figures (6) and (7) show the whirl ratio. Tests are done at two different rotor speeds to access the Reynolds Number effects. The 2000 RPM runs are shown first since they give the results at a lower flow coefficient range. A comparison of Figures (4) and (5) show differences between corresponding coefficient plots at the lower flow coefficients indicating that Reynolds Number effects are important at low flow rates. At flow coefficients above about 0.03 there seems to be little difference between corresponding coefficient plots at 1000 and 2000 RPM. Reynolds Number effects are stronger with no brake ribs installed. C and k seem to have the greatest discrepencies between the 1000 and 2000 RPM runs.

Focusing on the coefficients corresponding to the tangential force, we can see that with no brakes the tangential force decreases with increasing leakage flow rate, as was found previously by Guinzburg, (1992a). The cross-coupled stiffness coefficient, k, is decreased by increasing the flow from 0 to 30 GPM, and for the 1000 RPM case, C remains essentially constant. Hence the range for which the tangential force is destabilizing, k/C, decreases with increasing flow rate. This can be seen in Figure (7). However, looking at k for the case with 4 or 8 brake ribs, the opposite trend with flow rate is observed. The cross-coupled stiffness increases as the flow rate increases from 0 to 30 GPM in both the 1000 and 2000 RPM runs. The above may appear to indicate that brakes are not beneficial. On the contrary, although the destabilizing tangential force with brakes increases with flow rate, there is a flow rate below which the tangential force with brakes is less than the tangential force without brakes. From the k plots in Figures (4) and (5) we can see that below $\phi = 0.025$ the cross-coupled stiffness coefficient is reduced by the addition of 4 or 8 brakes. 8 brakes are only marginally more effective than 4. The beneficial effect of brakes is better exemplified by looking at the whirl ratio plots in Figures (6) and (7). Below about $\phi = 0.03$, the range of destabilizing tangential force is much less with the addition of brakes.

Focusing on the coefficients corresponding to the normal force, we can see that with no brakes, the normal force increases with increasing leakage flow rate. K becomes more negative with increasing flow, hence increasing the normal force at zero whirl frequency and therfore is destabilizing. The same is true with 4 or 8 brakes, but we can also see from K that the destabilizing normal force is significantly reduced by the addition of brakes throughout the range of flow rates tested.
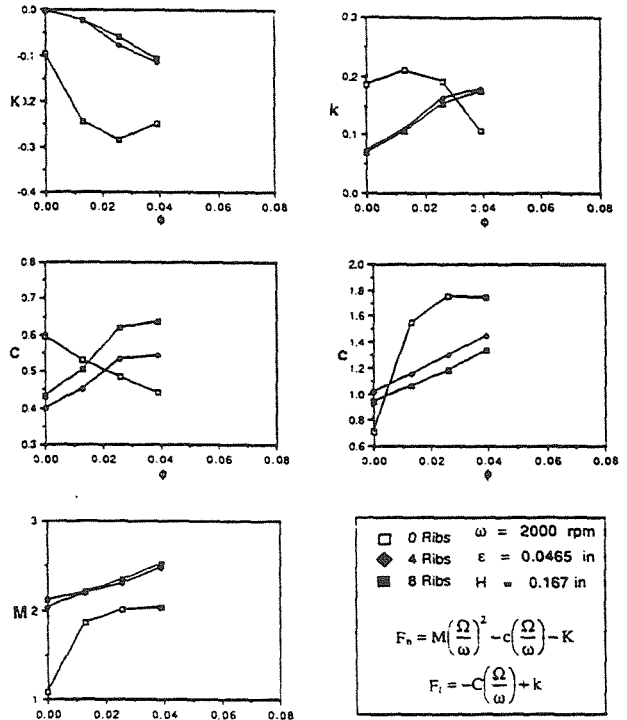

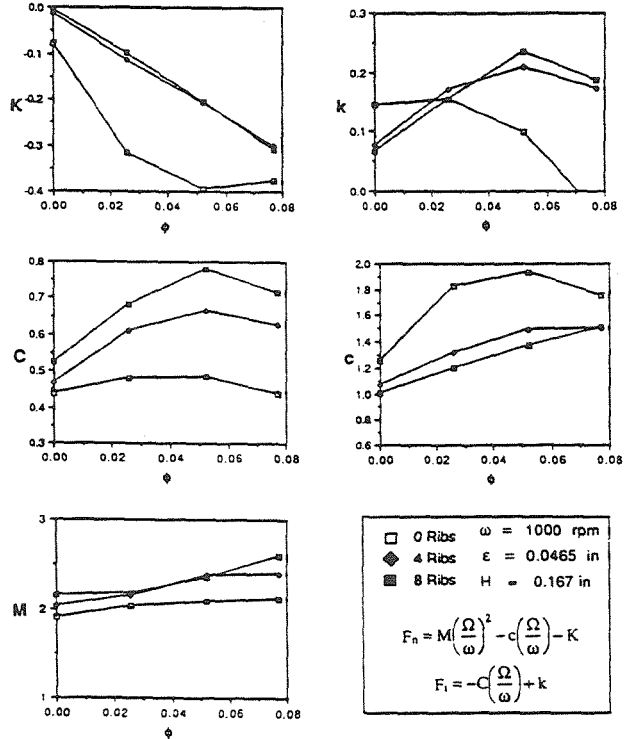FIGURE 4. ROTORDYNAMIC COEFFICIENTS AT 2000 RPM, NO SWIRL.

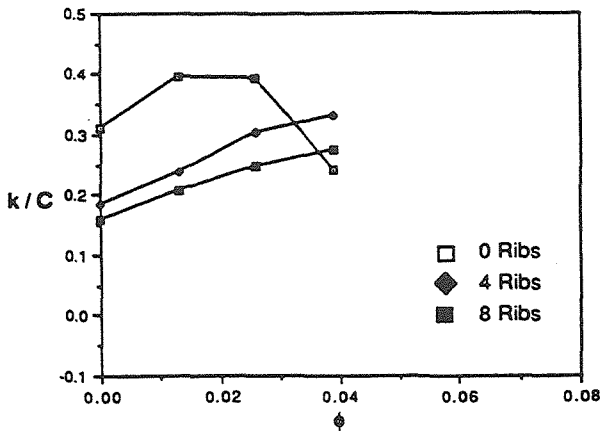FIGURE 5. ROTORDYNAMIC COEFFICIENTS AT 1000 RPM, NO SWIRL.

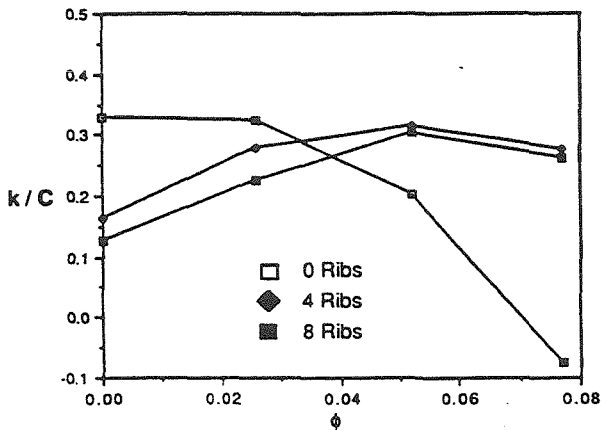FIGURE 6. WHIRL RATIO AT 2000 RPM, NO SWIRL.

FIGURE 7. WHIRL RATIO AT 1000 RPM, NO SWIRL.

RESULTS FOR TESTS WITH LEAKAGE INLET SWIRL

Figure (8) shows plots of the dimensionless rotordynamic coefficients for the 2000 RPM runs with leakage inlet swirl for the three different number of ribs. Figure (9) shows the whirl ratio. As was previously found by Guinzburg, (1992b), swirl dramatically increases the tangential force. This is evident by comparing the plot of k without swirl from Figure (4) with the plot of k with swirl from Figure (8). Once again, with no brakes, it can be seen that as the leakage rate increases, the tangential forces decrease, even though in the process the swirl ratio is increased. The stabilizing effect of an increase in flow rate dominates the destabi-

lizing effect of an increase in swirl ratio. When 4 or 8 brake ribs are used, the opposite trend with flow rate is observed, as shown with the results without swirl. With brakes, the tangential force increases with flow rate and swirl ratio. But, for the entire flow range tested, the cross-coupled stiffness is decreased by the addition of brakes.

Focusing on the coefficient K corresponding to the normal force, K is much large in the presence of swirl. We can see that with no brakes the normal force increases with increasing leakage flow rate. The same is true with 4 or 8 brakes, although from K, the destabilizing normal force is significantly reduced by the addition of brakes throughout the range of flow rates tested.

The most dramatic beneficial effect of brakes is found by comparing the whirl ratio plots for 4 or 8 brakes without and with swirl, figures (6) and (9), respectively. The 4 or 8 brake runs with and without swirl are almost identical. This indicates that the brakes almost completely eliminated the effect of swirl. With brakes present, swirl produces only a slight increase in the range for which the tangential force is destabilizing. Also, looking at Figure (9), for all flow rates tested, the addition of brakes reduces the range for which the tangential force is destabilizing.
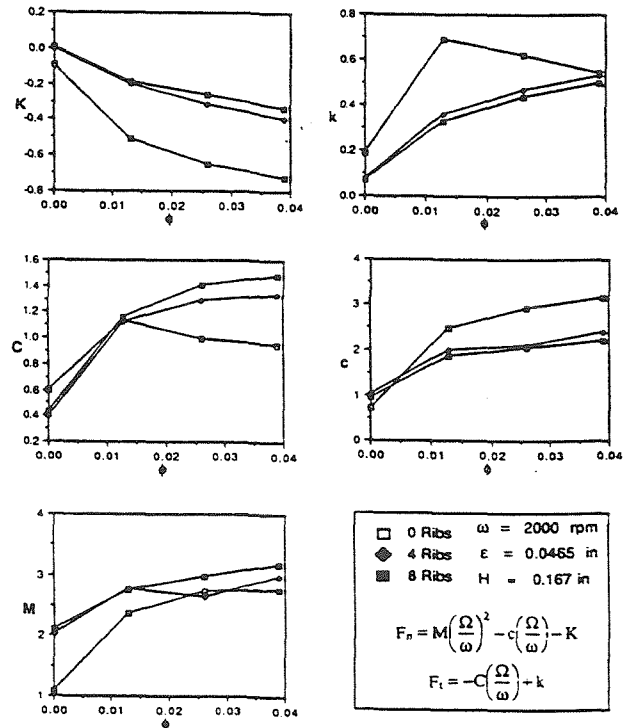

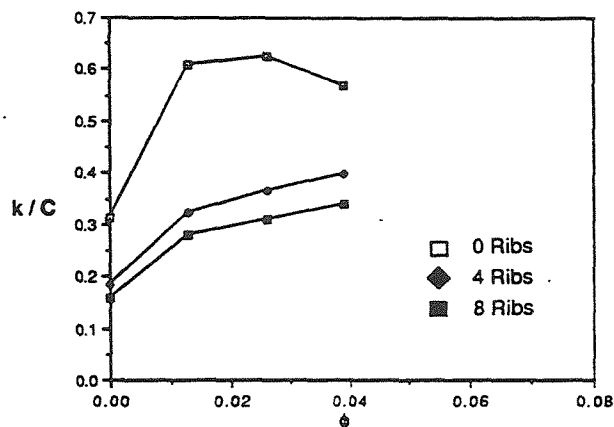FIGURE 8. ROTORDYNAMIC COEFFICIENTS AT 2000 RPM WITH SWIRL.

FIGURE 9. WHIRL RATIO AT 2000 RPM WITH SWIRL.

CONCLUSIONS

The influence of swirl brakes on the rotordynamic forces generated by discharge-to-suction leakage flows in centrifugal pumps with and without leakage inlet swirl has been investigated. The destabilizing normal force at zero whirl is reduced by the addition of brakes. The tangential force and the range of whirl frequency ratios for which the tangential force is destabilizing is reduced by the addition of brakes for low leakage flow rates. Brakes are beneficial in reducing the tangential force up to a higher leakage flow rate in the presence of leakage inlet swirl. Finally, the increase in the range of whirl frequency ratios for which the tangential force is destabilizing due to an increase in the leakage inlet swirl is nearly eliminated by the addition of swirl brakes.

ACKNOWLEDGEMENTS

REFERENCES

Adkins, D. R. and Brennen, C. E., 1988, Analysis of Hydrodynamic Radial Forces on Centrifugal Pump Impellers, ASME J. Fluids Eng., Vol. 110, No. 1, pp. 20-28.

Childs, D. W., Baskharone, E. and Ramsey, C., 1990, Test Results for Rotordynamic Coefficients of the SSME HPOTP Turbine Interstage Seal with Two Swirl Brakes, Trans of ASME, Journal of Tribology, 90-Trib-45.

Franz, R. J., 1989, Experimental Investigation of the Effect of Cavitation on the Rotordynamic Forces on a Whirling Centrifugal Pump Impeller, Ph.D. Thesis, California Institute of Technology.

Guinzburg, A., 1992a, Rotordynamic Forces Generated By Discharge-To-Suction Leakage Flows in Centrifugal Pumps, Ph.D. Thesis, California Institute of Technology.

Guinzburg, A., 1992b, The Effect of Inlet Swirl on the Rotordynamic Shroud Forces in a Centrifugal Pump, ASME Paper 92-GT-126.

Jery, B., 1986, Experimental Study of Unsteady Hydrodynamic Force Matrices on Whirling Centrifugal Pump Impellers, Ph.D. Thesis, California Institute of Technology.

Zhuang, F., 1989, Experimental Investigation of the Hydrodynamic Forces on the Shroud of a Centrifugal Pump Impeller, E249.9, Division of Engineering and Applied Science, California Institute of Technology.

FED-Vol. 154

PUMPING MACHINERY 1993

presented at
THE FLUIDS ENGINEERING CONFERENCE
WASHINGTON, D.C.
JUNE 20-24, 1993

sponsored by
THE FLUIDS ENGINEERING DIVISION, ASME

edited by
PAUL COOPER
INGERSOLL-DRESSER PUMP CO.

Chapter 2

Laser Velocimeter Measurements in the Leakage Annulus of a Whirling Shrouded Centrifugal Pump

LASER VELOCIMETER MEASUREMENTS IN THE LEAKAGE ANNULUS
OF A WHIRLING SHROUDED CENTRIFUGAL PUMP

J. M. Sivo, A. J. Acosta, C. E. Brennen, and T. K. Caughey
Division of Engineering and Applied Science
California Institute of Technology
Pasadena, California

T. V. Ferguson and G. A. Lee
Rocketdyne Division
Rockwell International Corporation
Canoga Park, California

ABSTRACT

Previous experiments conducted in the Rotor Force Test Facility at the California Institute of Technology have thoroughly examined the effect of leakage flows on the rotordynamic forces on a centrifugal pump impeller undergoing a prescribed circular whirl. These leakage flows have been shown to contribute substantially to the total fluid induced forces acting on a pump. However, to date nothing is known of the flow field in the leakage annulus of shrouded centrifugal pumps. No attempt has been made to qualitatively or quantitatively examine the velocity field in the leakage annulus. Hence the test objective of this experiment is to aquire fluid velocity data for a geometry representative of the leakage annulus of a shrouded centrifugal pump while the rotor is whirling using laser velocimetry. Tests are performed over a range of whirl ratios and a flowrate typical of Space Shuttle Turbopump designs. In addition to a qualitative study of the flow field, the velocity data can be used to anchor flow models.

NOMENCLATURE

d	Location across leakage gap measured normal from impeller shroud
H	Clearance between impeller shroud and housing
Q	Volumetric leakage flow rate
ϵ	Eccentricity of impeller's circular whirl orbit
ω	Main shaft radian frequency
Ω	Whirl radian frequency

INTRODUCTION

Previous experimental and analytical results have shown that discharge-to-suction leakage flows in the annulus of a shrouded centrifugal pump contribute substantially to the fluid induced rotordynamic forces (Adkins, 1988). Experiments conducted in the Rotor Force Test Facility (RFTF) at Caltech on an impeller undergoing a prescribed whirl have indicated that the leakage flow contribution to the normal and tangential forces can be as much as 70% and 30% of the total, respectively (Jery, 1986). Recent experiments at Caltech have examined the rotordynamic consequences of leakage flows and have shown that the rotordynamic forces are functions not only of the whirl ratio but also of the leakage flow rate and the impeller shroud to pump housing clearance. The forces were found to be inversely proportional to the clearance and a region of forward subsynchronous whirl was found for which the average tangential force was destabilizing. This region decreased with flow coefficient (Guinzburg, 1992a). In recent experimental work, the present Caltech authors demonstrated that when the swirl velocity within the leakage path is reduced by the introduction of ribs or swirl brakes on the housing, then a substantial decrease in both the destabilizing normal and tangential forces could be achieved (Sivo, 1993).The motivation for the present research is that no previous experiments have examined the flow field within the leakage annulus. No measurements have been made of the destabilizing swirl or tangential velocity or demonstrated the complex nature of the flow. Analytical models of such flows use bulk average velocities to examine the rotordynamic forces. Such bulk flow models may be seriously flawed

when it comes to estimating the meridional and tangential velocities. It is hoped that this present research will serve as preliminary insight into the complex nature of leakage flows.

TEST APPARATUS

The present experiments were conducted in the Rotor Force Test Facility (RFTF) at Caltech and were sponsored by Rocketdyne. The leakage flow test section of the facility is shown in Figure (1).

The working fluid is water. The main components of the test section apparatus consist of a solid or dummy impeller (or rotating shroud) made of acrylic, a housing (or stationary shroud) instrumented for pressure measurements, a rotating dynamometer (or internal force balance), an eccentric whirl mechanism (not shown) and a leakage exit seal ring. The solid acrylic impeller is used so that backscatter to the velocimeter is minimized. The surface of the stationary housing has been modified to accommodate an optical flat glass window to view the fluid in the annulus. The leakage flow annulus between the impeller and housing is inclined at 45° to the axis of rotation. The nominal clearance between the solid impeller and the housing can be varied by axial adjustment of the housing. The flow through the leakage path is generated by an auxiliary pump. The solid impeller is mounted on a spindel attached to the rotating dynamometer connected to a data acquisition system which permits measurements of the rotordynamic force matrix. Jery, 1986 and Franz, 1989 describe the operation of the dynamometer. The eccentric drive mechanism imposes a circular whirl orbit on the basic main shaft rotation. The radius of the circular whirl orbit (or eccentricity) can be varied. The seal ring at the leakage exit models a wear ring. The clearance between the seal ring and impeller face is adjustable. The test approach makes use of the Rocketdyne Laser 2-focus Velocimeter to aquire fluid velocities across the shroud cavity. A pseudo-time history is obtained by using the velocimeter's multi-windowing synchronizer capability. This time history allows correlation of the velocity data to the rotor whirl.

A Polytec model 4000 laser-2-focus (L2F) velocimeter was used to conduct the testing. This two-spot or transit type velocimeter employed a 1 watt argon ion laser in an optical head with a 450 mm focal length lens. During testing the laser was operated at a lower power level resulting in about 125 mW in each spot. The L2F acquired data in a coaxial backscatter mode which was a requirement given the physical constraints of the tester hardware. The electronic signal processing sub-section of the velocimeter included an
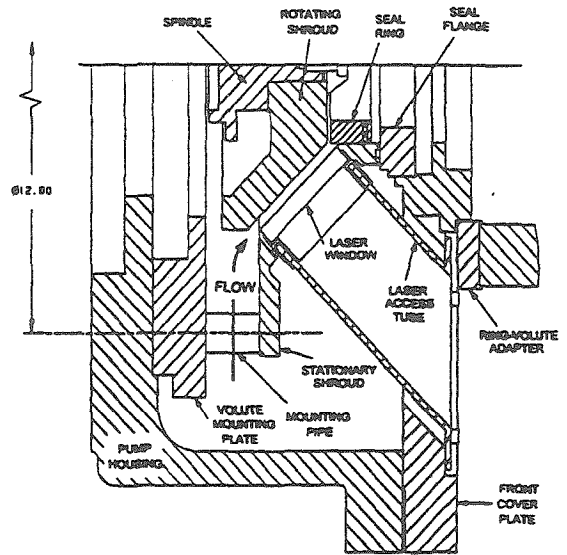

FIGURE 1. LEAKAGE FLOW TEST SECTION

analog time-to-pulse-height converter with a multichannel analyzer for display and accumulation of the data. Final reduction of the data was performed on a PC utilizing data reduction software from Polytec. Velocity and flow angles calculated from the time-of-flight and angular distributions, respectively, were output.

The L2F velocimeter in conjunction with an electronic synchronizer tagged the velocity and flow angle data relative to the whirl frequency of the impeller. Phase lock signals from the motor drive electronics were input to a strobe light. The rotating tester was viewed under the strobe light to determine the orbital position of the rotor when the whirl signal was generated. Sixteen circumferential zones or windows were generated by the synchronizer. Each window represents 22.5 degrees of rotation of the rotor during its whirl period. Therefore each window represents a pseudo-time history of the annulus flow as the orbital eccentricity of the impeller alternately squeezes and restores the nominal dimensions of the flow passage. The velocity and flow angle in each of these 16 windows was determined by the L2F.

The velocimeter was setup so the beams from the optical head were normal to the optical access window and concurrently to the surface of the impeller. Measurements were made in the plane normal to the propagation of the beam. The stop spot rotated about the start spot in this plane in order to explore for the direction of the flow vector.

The axial length of the measurement volumes was determined by the steep intensity gradient along the

beam axis. The measurement volume length can be defined as the space bounded by the points where the intensity in the beam was one-fourth of the maximum intensity at the waist, or in other words, where the beam radius has doubled. Using this definition, the length of the measurement volume was calculated to be 0.76 mm (0.030 inch).

The data were acquired through a rectangular-shaped window approximately 2.5 inches in length, 0.5 inches in height and 0.5 inches thick. The optical head (and hence the measurement volumes) was aligned with the test hardware by monitoring the speckle pattern reflected from the metal boundaries in the test hardware and the window frame. The accuracy of the speckle alignment data was validated by measurements made with depth micrometers. In addition, measurements were performed to assure the optical head was oriented normal to the optical access window so that the data collected across the annulus was in the same plane. Other measurements assured the head tracked level along the length of the window and that the relative angle between the zero angle position of the spots and the test hardware was quantified.

To improve the signal-to-noise ratio of the velocimeter measurements, the fluid was supplementally seeded with silver coated hollow glass micro-spheres. The mean particle size was 14 microns and the particle density was 1.4 gm/cm^3. A small quantity of the dry powdered spheres were mixed with distilled water. About 40-100 cc of this slurry was injected with a syringe into a pressure port located downstream of the test article. The particles, typically injected just before data collection at each measurement station, would circulate for about one hour in the closed loop test rig before settling out.

The L2F excels at measuring flows characterized by high velocity and low turbulence particularly in turbomachinery. Its performance efficiency in low velocity, high turbulence flows exemplified by this testing was not as good. A sufficient quantity of data was required for good statistical analysis of the time- of-flight and angular distributions in each of the 16 windows. Consequently, long run times were necessary. The information in Table 1 illustrates some of the parameters of the test. Overall, the number of data samples in each of the 16 windows was sufficient to yield an accuracy of at least $+/-2\%$ in velocity and generally closer to $+/-1\%$. The flow angle data is accurate to about $+/-1$ degree.

TEST MATRIX

This experiment is designed to measure the velocity of simulated leakage flows for different parameters

such as whirl frequency ratio, axial location, and leakage annulus depth. For all tests a nominal annulus clearance H of 0.1072 in, a whirl eccentricity ε of 0.01in and a leakage exit face seal clearance of 0.02 in were maintained. Tests were conducted at a shaft speed ω of 2000 RPM and a leakage flow rate Q of 10 GPM. The above flow approximates the range of typical leakage rates for the new Space Shuttle Alternate Turbopump (ATP) presently being developed. Whirl ratios Ω/ω of 0.2, 0.3, 0.4 were tested. Velocity measurements were made at three meridional locations along the leakage path: Near Inlet (.6054 in), Near Midpoint (1.4054 in), Near Discharge (2.4054 in). The leakage path length along the impeller is 2.74 in. At each of these three stations, measurements were made at 5 depth locations across the leakage gap. Measuring from the solid impeller these positions were 0.0178 in (16.7%), 0.0357 in (33.4%), 0.0536 in (50%), 0.0715 in (66.7%), and 0.0893 in (83.3%).

The above test matrix is summarized in Table 2.

Table 1. Parameters of the Tests

whirl ratio	approximate average number of angles in a scan	average number of samples per angle	average data collection time (sec)	number of whirls over which data was averaged
0.2	35	51.667	3581	23.885
0.3	42	50.000	3880	38.800
0.4	36	51.545	3851	51.346

Table 2. Velocimeter Measurements

RPM	Q (GPM)	Ω/ω	d (in)
2000	10	0.2	0.0178 (16.7%)
			0.0357 (33.4%)
			0.0536 (50.0%)
			0.0715 (66.7%)
			0.0893 (83.3%)
		0.3	0.0178 (16.7%)
			0.0357 (33.4%)
			0.0536 (50.0%)
			0.0715 (66.7%)
			0.0893 (83.3%)
		0.4	0.0178 (16.7%)
			0.0357 (33.4%)
			0.0536 (50.0%)
			0.0715 (66.7%)
			0.0893 (83.3%)

RESULTS FOR MEASUREMENTS OF MERIDIONAL VELOCITY

In the following results not all gap locations are reported. This is due to the low signal to noise ratio for gap locations near the impeller shroud surface.

Figure (2) shows plots of the absolute meridional velocity at a whirl ratio of 0.2 for the three meridional locations respectively. Looking at the Near Inlet figure it can be seen that reverse flow occurs for the 33.4% gap point between the whirl orbit angles of 110° and 260°. Further away from the impeller across the gap there is no reverse flow. Looking at the Near Mid-point figure reverse flow occurs again for the 33.4% gap point, but only for a smaller range of whirl orbit angles of 120° to 220°. Once again further away from the impeller across the gap there is no reverse flow. Looking at the Near Discharge figure, there is no evidence of reverse flow. Hence from the above it appears that there is recirculation near the surface of the impeller between the inlet to the leakage path and the midpoint.

Figure (3) shows similar plots except for a whirl ratio of 0.3. The Near Inlet figure shows that the 16.7% and 33.4% gap points are in reverse flow at all whirl orbit locations. For the Near Mid-point figure there is reverse flow between 120° and 200°. From the Near Discharge figure there is no evidence of reverse flow. Hence, once again it appears that there is a recirculation zone near the surface of the impeller between the inlet to the leakage path and the midpoint.

Figure (4) shows similiar plots except for a whirl ratio of 0.4. There is no evidence of recirculation, except in the Near Mid-point figure where there is recirculation for the 33.4% gap point at 150°.

As a general observation of all the above plots it can be seen that the meridional velocity is largest furthest from the rotating impeller and is quite large at the 83.3% gap point, which is closest to the stationary casing.

RESULTS FOR MEASUREMENTS OF TANGENTIAL VELOCITY

Figures (5) through (7) show the absolute tangential velocity for the three whirl ratios tested and five gap locations. A few general observations can be made. Near Inlet plots show the velocity profiles spread out with the largest tangential velocity nearest the impeller, as expected. Also except for the 0.4 whirl case, near discharge velocity profiles bunch up close to the impeller. It is as if a bulk tangential velocity is set up.

CONCLUSIONS

Laser velocimeter measurements have been made in the leakage annulus of a whirling shrouded impeller. Results clearly show regions of recirculation which diminish at higher whirl ratios. These recirculation regions are dominant near the entrance to the leakage path. In some cases these recirculation regions exist entirely around the impeller.

REFERENCES

Adkins, D. R. and Brennen, C. E., 1988, Analysis of Hydrodynamic Radial Forces on Centrifugal Pump Impellers, ASME J. Fluids Eng., Vol. 110, No. 1, pp. 20-28.

Franz, R. J., 1989, Experimental Investigation of the Effect of Cavitation on the Rotordynamic Forces on a Whirling Centrifugal Pump Impeller, Ph.D. Thesis, California Institute of Technology.

Guinzburg, A., 1992a, Rotordynamic Forces Generated By Discharge-To-Suction Leakage Flows in Centrifugal Pumps, Ph.D. Thesis, California Institute of Technology.

Jery, B., 1986, Experimental Study of Unsteady Hydrodynamic Force Matrices on Whirling Centrifugal Pump Impellers, Ph.D. Thesis, California Institute of Technology.

Sivo, J. M., Acosta, A. J., Brennen, C. E. and Caughey, T. K., 1993, The Influence of Swirl Brakes on the Rotordynamic Forces Generated by Discharge-To-Suction Leakage Flows in Centrifugal Pumps, presented at the ASME Second Pumping Machinery Symposium, Washington, D. C., June 20-24, 1993.

Zhuang, F., 1989, Experimental Investigation of the Hydrodynamic Forces on the Shroud of a Centrifugal Pump Impeller, E249.9, Division of Engineering and Applied Science, California Institute of Technology.
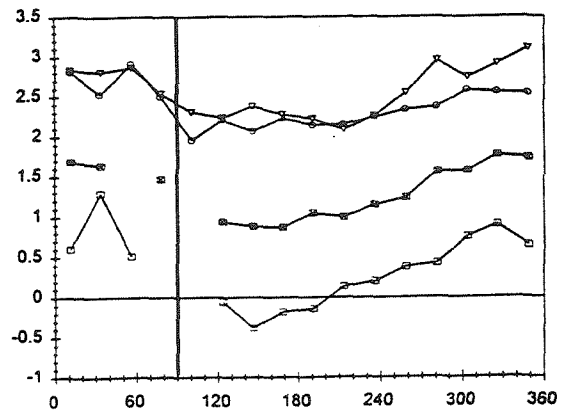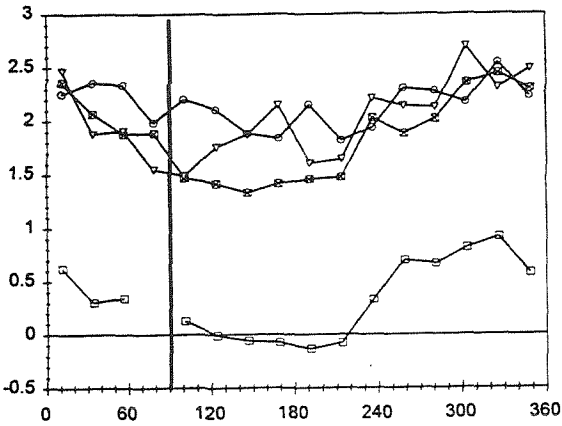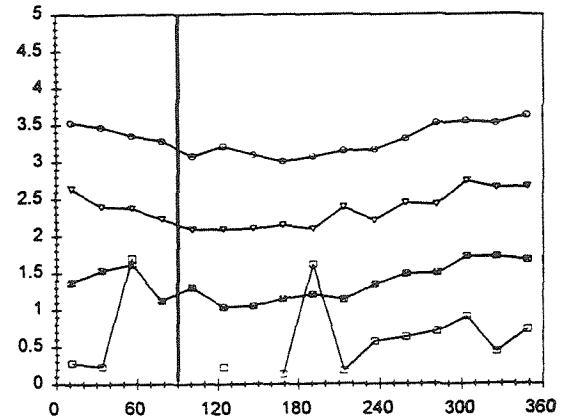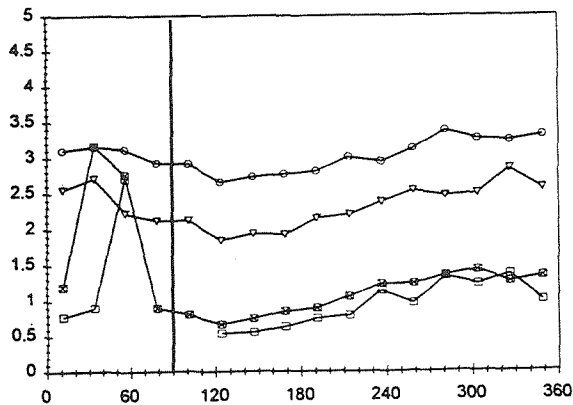
Meridional Velocity

LEGEND: Percentage across gap

● 16.7% □ 33.4% ⊠ 50% ▽ 66.7% ○ 83.3%

$\Omega/\omega = +0.2$

$\Omega/\omega = +0.3$
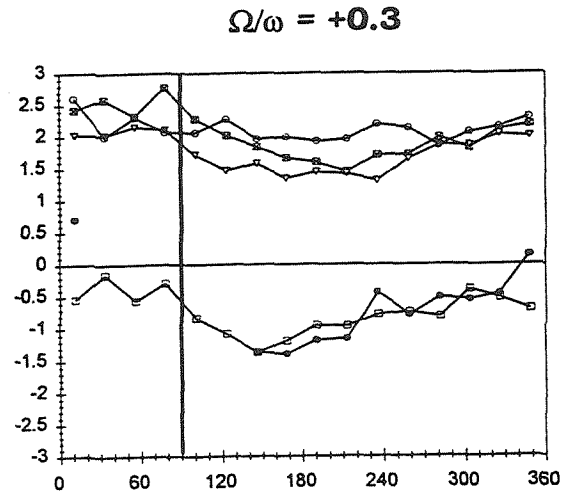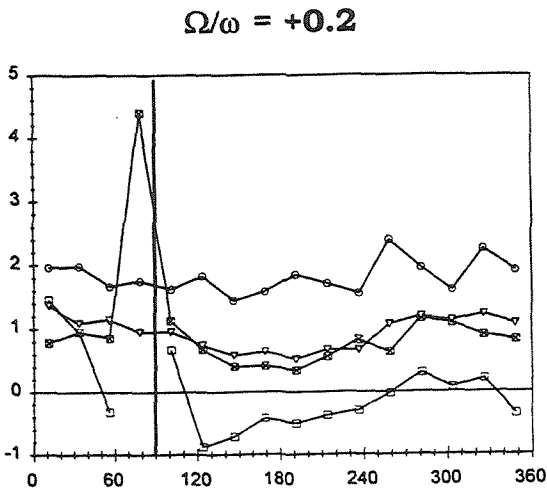
Near Inlet

Mid-Point

Near Discharge

Location in Whirl Orbit (deg)
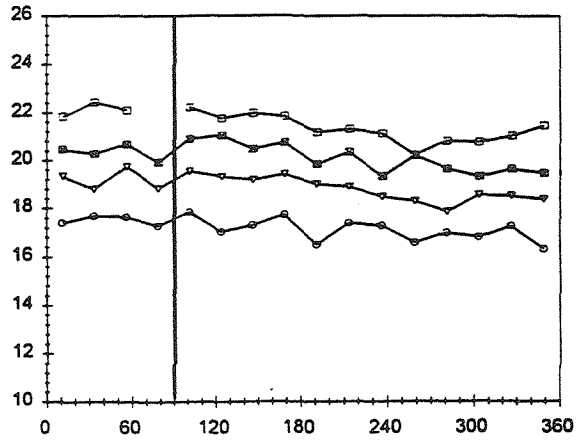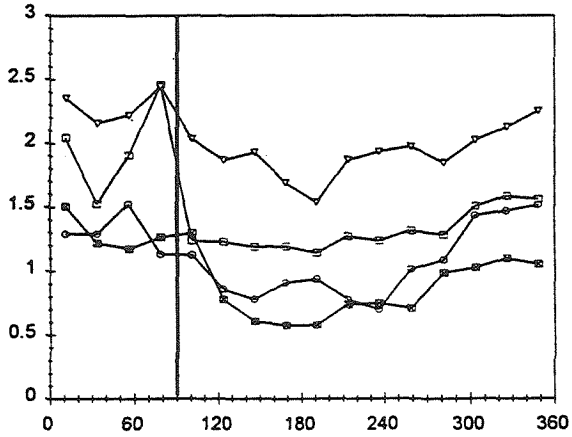
FIGURE 2.   115   FIGURE 3.

Meridional Velocity

Tangential Velocity

$\Omega/\omega = +0.4$

$\Omega/\omega = +0.2$

Near Inlet

Mid-Point
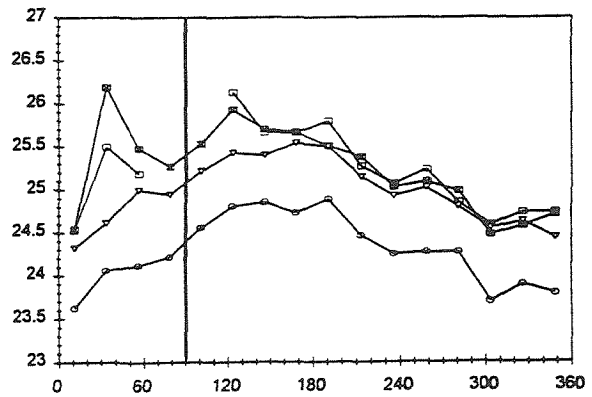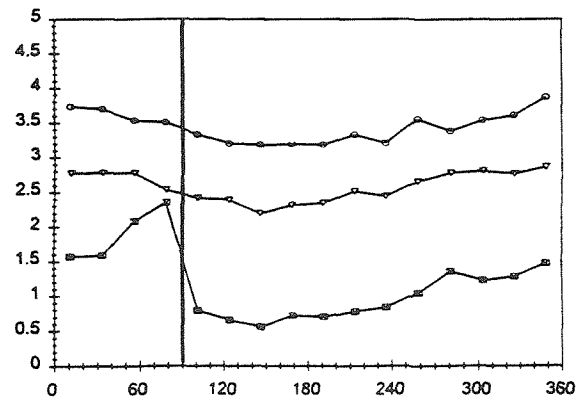
Near Discharge

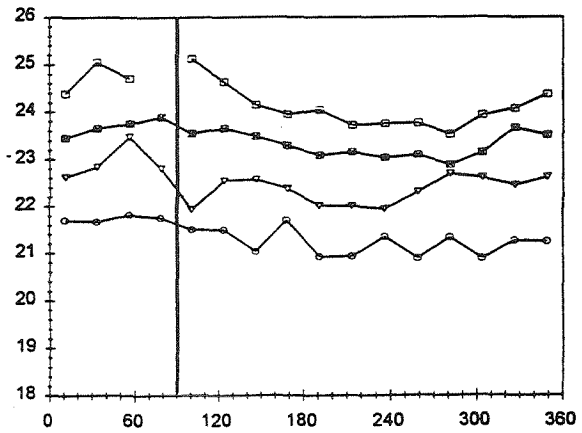**Location in Whirl Orbit (deg)**
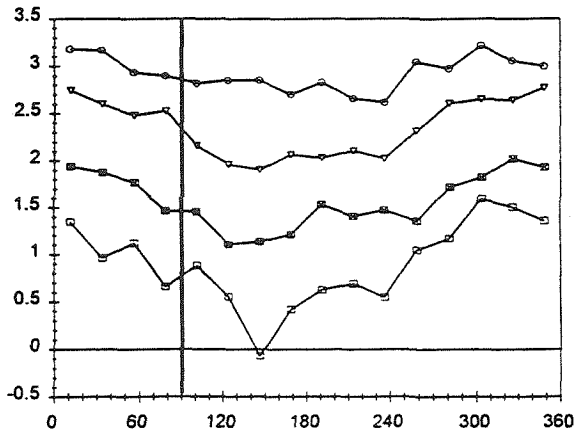
FIGURE 4.

FIGURE 5.

Tangential Velocity

$\Omega/\omega = +0.3$
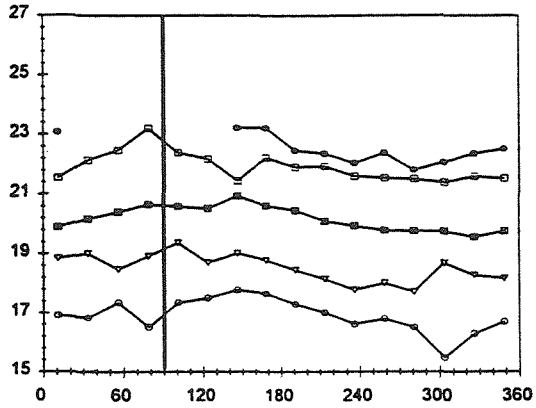
$\Omega/\omega = +0.4$
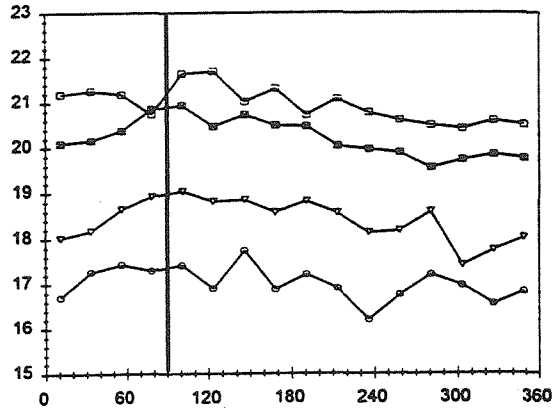
Near Inlet
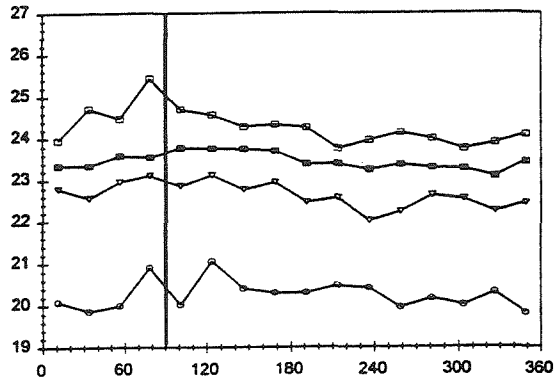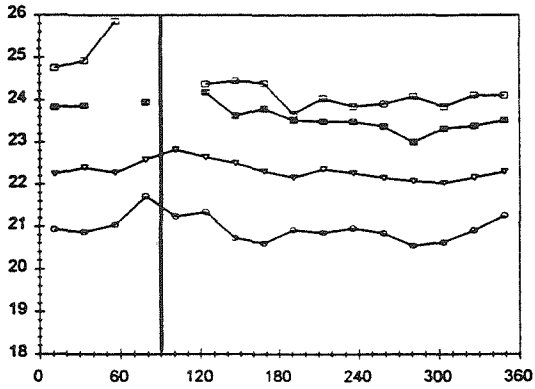
Mid-Point
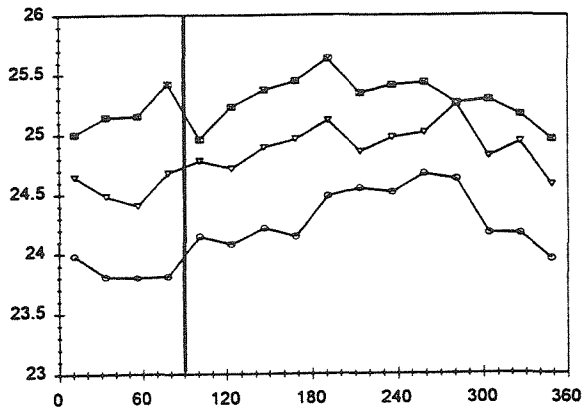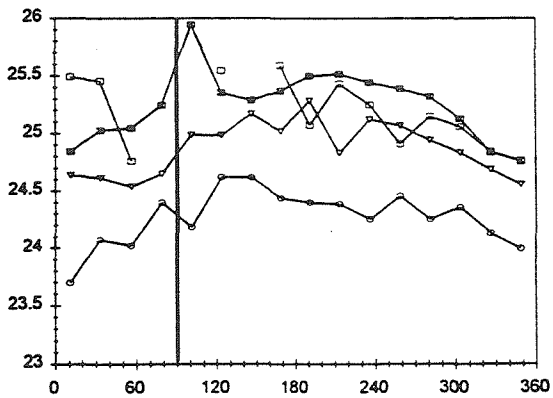
Near Discharge

Location in Whirl Orbit (deg)

FIGURE 6.

FIGURE 7.

LASER ANEMOMETRY
1994
ADVANCES AND
APPLICATIONS

edited by
T. T. Huang
David Taylor Model Basin

M. V. Otugen
Polytechnic University

Chapter 3

The Influence of Swirl Brakes and a Tip Discharge Orifice
on the Rotordynamic Forces Generated by
Discharge-to-Suction Leakage Flows in Shrouded Centrifugal Pumps

The Influence of Swirl Brakes on the Rotordynamic Forces Generated by Discharge-to-Suction Leakage Flows in Centrifugal Pumps

J. M. Sivo

A. J. Acosta

C. E. Brennen

T. K. Caughey

Division of Engineering
and Applied Science,
California Institute of Technology,
Pasadena, CA 91125

Increasing interest has been given to swirl brakes as a means of reducing desta-bilizing rotordynamic forces due to leakage flows in new high speed rocket turbo-pumps. Although swirl brakes have been used successfully in practice (such as with the Space Shuttle HPOTP), no experimental tests until now have been performed to demonstrate their beneficial effect over a range of leakage flow rates. The present study investigates the effect of swirl brakes on rotordynamic forces generated by discharge-to-suction leakage flows in the annulus of shrouded centrifugal pumps over a range of subsynchronous whirl ratios and various leakage flow rates. In addition, the effectiveness of swirl brakes in the presence of leakage inlet (pump discharge) swirl is also demonstrated. The experimental data demonstrates that with the addition of swirl brakes a significant reduction in the destabilizing tangential force for lower flow rates is achieved. At higher flow rates, the brakes are detri-mental. In the presence of leakage inlet swirl, brakes were effective over all leakage flow rates tested in reducing the range of whirl frequency ratio for which the tan-gential force is destabilizing.

Introduction

Previous experimental and analytical results have shown that discharge-to-suction leakage flows in the annulus of a shrouded centrifugal pump contribute substantially to the fluid induced rotordynamic forces (Adkins, 1988). Experiments conducted in the Rotor Force Test Facility (RFTF) at Caltech on an im-peller undergoing a prescribed whirl have indicated that the leakage flow contribution to the normal and tangential forces can be as much as 70 and 30 percent of the total, respectively (Jery, 1986). Recent experiments at Caltech have examined the rotordynamic consequences of leakage flows and have shown that the rotordynamic forces are functions not only of the whirl ratio but also of the leakage flow rate and the impeller shroud to pump housing clearance. The forces were found to be in-versely proportional to the clearance and a region of forward subsynchronous whirl was found for which the average tan-gential force was destabilizing. This region decreased with flow coefficient (Guinzburg, 1992a).

The motivation for the present research is that the previous experiments have shown that leakage inlet (pump discharge) swirl can increase the cross-coupled stiffness coefficient (in

some tests by over 100 percent) and hence increase the range of positive whirl for which the tangential force is destabilizing. One might therefore surmise that if the swirl velocity within the leakage path were reduced, then the destabilizing tangen-tial force might be reduced. One way of reducing the leakage flow swirl is with the use of ribs or swirl brakes on the hous-ing. In fact, swirl brakes installed upstream of the interstage seal on the Space Shuttle Main Engine High Pressure Oxygen Turbopump completely eliminated the subsynchronous whirl motion over the steady state operating range of the unit (Childs, 1990). The present study investigates the influence of swirl brakes on the rotordynamic forces generated by discharge-to-suction leakage flows in shrouded centrifugal pumps over a range of subsynchronous whirl ratios and various leakage flow rates typical of present rocket turbopump designs. In addition, the effectiveness of swirl brakes in the presence of leakage inlet (pump discharge) swirl is also demonstrated.

Rotordynamic Forces

Figure 1 shows a schematic of the hydrodynamic forces that act on a rotating impeller whirling in a circular orbit. F_x^* and F_y^* are the instantaneous lateral forces in the laboratory frame. Ω is the whirl radian frequency and ω is the main shaft radian frequency. The eccentricity of the orbit is given by ϵ. The
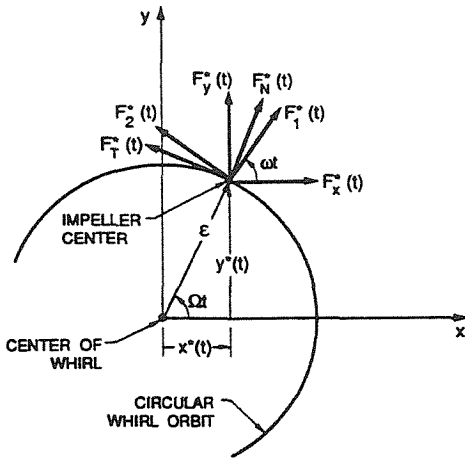
Fig. 1 Schematic of the fluid-induced forces acting on an impeller whirling in a circular orbit

lateral forces are given in linear form as:

$$\begin{pmatrix} F_x^*(t) \\ F_y^*(t) \end{pmatrix} = \begin{pmatrix} F_{ox}^* \\ F_{oy}^* \end{pmatrix} + [A^*]\begin{pmatrix} x^*(t) \\ y^*(t) \end{pmatrix} \qquad (1)$$

F_{ox}^* and F_{oy}^* are the steady forces which result from flow asymmetries in the volute. $[A^*]$ is the rotordynamic force matrix. It is a function of the mean flow conditions, pump geometry, whirl frequency ratio Ω/ω and if outside the linear range it may also be a function of the eccentricity ϵ. In the case of a circular whirl orbit:

$$x^*(t) = \epsilon \cos(\Omega t) \qquad (2)$$

$$y^*(t) = \epsilon \sin(\Omega t) \qquad (3)$$

The normal and tangential forces for a circular whirl orbit are given by (Jery, 1986 and Franz 1989):

$$F_n^*(t) = \frac{1}{2}(A_{xx}^* + A_{yy}^*)\epsilon \qquad (4)$$

$$F_t^*(t) = \frac{1}{2}(-A_{xy}^* + A_{yx}^*)\epsilon \qquad (5)$$

Rotordynamic Coefficients and Stability

To study the stability of an impeller, it is convenient for rotordynamicists to fit the dimensionless normal force F_n to a

quadratic function of the whirl ratio and to fit the dimensionless tangential force F_t to a linear function of the whirl ratio. The expressions are given by:

$$F_n = M\left(\frac{\Omega}{\omega}\right)^2 - c\left(\frac{\Omega}{\omega}\right) - K \qquad (6)$$

$$F_t = -C\left(\frac{\Omega}{\omega}\right) + k \qquad (7)$$

where the dimensionless coefficients are the direct added mass (M), direct damping (C), cross-coupled damping (c), direct stiffness (K), and cross-coupled stiffness (k). As can be seen from (7), a positive cross-coupled stiffness is destabilizing because it starts the forward whirl of the impeller since it is equal to the tangential force at zero whirl ratio. Also, from (6), a large negative direct stiffness is destabilizing because it promotes a positive normal force which increases the eccentricity of the whirl orbit.

A convenient measure of the rotordynamic stability is the ratio of the cross-coupled stiffness to the direct damping (i.e., k/C) termed the whirl ratio. This is just a measure of the range of positive whirl frequency ratios for which the tangential force is destabilizing.

Test Apparatus

The present experiments were conducted in the Rotor Force Test Facility (RFTF) at Caltech. The leakage flow test section of the facility is shown in Fig. 2.

The working fluid is water. The main components of the test section apparatus consist of a solid or dummy impeller (or rotating shroud), a housing (or stationary shroud) instrumented for pressure measurements, a rotating dynamometer (or internal force balance), an eccentric whirl mechanism (not shown), a leakage exit seal ring and a leakage inlet swirl vane (shown installed in Fig. 3). The solid impeller is used so that leakage flow contributions to the forces are measured but the main through flow contributions are not experienced. The inner surface of the housing has been modified to accommodate meridional ribs or swirl brakes along the entire length of the leakage annulus. The ribs are each 3/16 of an inch wide and 2 mm high. Up to 8 equally spaced ribs can be installed. The leakage flow annulus between the impeller and housing is inclined at 45 deg to the axis of rotation. The nominal clearance between the solid impeller and the housing can be varied by axial adjustment of the housing. The flow through the leakage path is generated by an auxiliary pump. The solid impeller is

Nomenclature

$[A^*]$ = rotordynamic force matrix

B = depth of logarithmic spiral channel on swirl vane

c = cross-coupled damping coefficient, normalized by $\rho\pi\omega^2 R_2^2 L\epsilon$

C = direct damping coefficient, normalized by $\rho\pi\omega^2 R_2^2 L\epsilon$

$F_x^*(t)$ = lateral horizontal force in the laboratory frame

$F_y^*(t)$ = lateral vertical force in the laboratory frame

F_{ox}^* = steady horizontal force

F_{oy}^* = steady vertical force

F_n^* = force normal to whirl orbit

F_n = force normal to whirl orbit normalized by $\rho\pi\omega^2 R_2^2 L\epsilon$

F_t^* = force tangent to whirl orbit

F_t = force tangent to whirl orbit normalized by $\rho\pi\omega^2 R_2^2 L\epsilon$

F_1, F_2 = lateral forces in rotating frame

H = clearance between impeller shroud and housing

k = cross-coupled stiffness coefficient normalized by $\rho\pi\omega^2 R_2^2 L\epsilon$

K = direct stiffness coefficient normalized by $\rho\pi\omega^2 R_2^2 L\epsilon$

L = axial length of impeller

M = direct added mass coefficient normalized by $\rho\pi\omega^2 R_2^2 L\epsilon$

Q = volumetric leakage flow rate

R_2 = radius of impeller at leakage inlet

u_s = mean leakage inlet path velocity of fluid

u_θ = mean leakage inlet swirl velocity of fluid

$x^*(t)$ = horizontal displacement of impeller on its orbit

$y^*(t)$ = vertical displacement of impeller on its orbit

α = turning angle of logarithmic spiral channel on swirl vane

Γ = leakage inlet swirl ratio, $u_\theta/\omega R_2$

ϵ = eccentricity of impeller's circular whirl orbit

ρ = density of leakage fluid

ϕ = leakage flow coefficient, $u_s/\omega R_2$

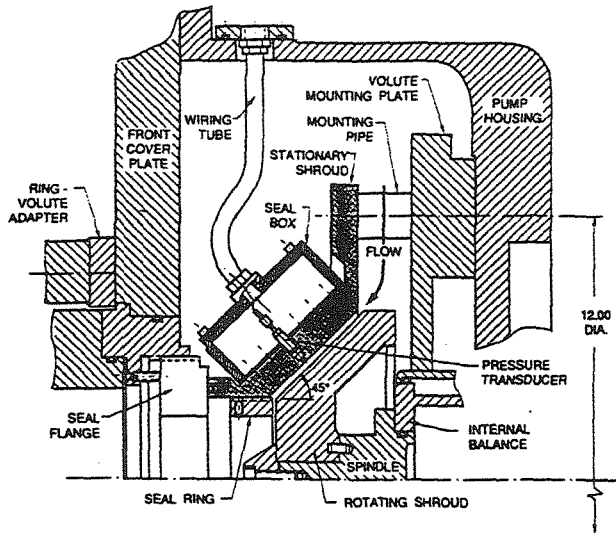ω = main shaft radian frequency

Ω = whirl radian frequency
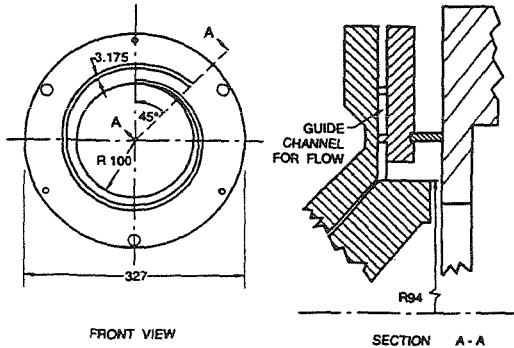
Fig. 2 Leakage flow test section (Zhuang, 1989)

Fig. 3 Installation of leakage inlet swirl vane. Dimensions in mm (Guinzburg, 1992b)

Table 1 Tests without swirl

rpm	Ω/ω	Brakes	Q (GPM)	ϕ
1000	−0.9 to +0.9	0	0	0.0
			10	0.026
			20	0.052
			30	0.077
		4	0	0.0
			10	0.026
			20	0.052
			30	0.077
		8	0	0.0
			10	0.026
			20	0.052
			30	0.077
2000	−0.6 to +0.7	0	0	0.0
			10	0.013
			20	0.026
			30	0.039
		4	0	0.0
			10	0.013
			20	0.026
			30	0.039
		8	0	0.0
			10	0.013
			20	0.026
			30	0.039

Table 2 Tests with swirl

rpm	Ω/ω	Brakes	Q (GPM)	ϕ	Γ
2000	−0.6 to +0.7	0	0	0.0	0.0
			10	0.013	0.5
			20	0.026	1.0
			30	0.039	1.5
		4	0	0.0	0.0
			10	0.013	0.5
			20	0.026	1.0
			30	0.039	1.5
		8	0	0.0	0.0
			10	0.013	0.5
			20	0.026	1.0
			30	0.039	1.5

mounted on a spindel attached to the rotating dynamometer connected to a data acquisition system which permits measurements of the rotordynamic force matrix. Jery (1986) and Franz (1989) describe the operation of the dynamometer. The eccentric drive mechanism imposes a circular whirl orbit on the basic main shaft rotation. The radius of the circular whirl orbit (or eccentricity) can be varied. The seal ring at the leakage exit models a wear ring. The clearance between the seal ring and impeller face is adjustable. The effect of swirl was investigated by installing a swirl vane at the leakage inlet to introduce prerotated fluid in the direction of shaft rotation. Figure 3 shows that the vane consists of a logarithmic spiral channel with a turning angle of 2 deg. The swirl ratio Γ (the ratio of the leakage flow circumferential velocity to the impeller tip velocity) is varied by changing the leakage flow rate. The swirl ratio depends on the flow coefficient according to:

$$\frac{\Gamma}{\phi} = \frac{H}{B \, \mathrm{Tan}(\alpha)} \tag{8}$$

B is the depth of the logarithmic spiral channel equal to 0.125 in. A derivation of Eq. (8) can be found in Guinzburg (1992a).

Test Matrix

This experiment is designed to measure the rotordynamic forces due to simulated leakage flows for different parameters such as whirl frequency ratio, shaft speed, leakage flow coefficient, number of swirl brake ribs and leakage inlet swirl ratio. For all tests a nominal annulus clearance H of 0.167 in, a whirl eccentricity ϵ of 0.0465 in and a leakage exit face seal clearance of 0.04 in were maintained. Tests without leakage inlet swirl were conducted at shaft speeds ω of 1000 and 2000 rpm, leakage flow rates Q of 0, 10, 20, and 30 GPM and 0, 4, and 8 brake ribs. For the 1000 rpm runs, the above flow rates correspond to flow coefficients ϕ of 0.0, 0.026, 0.052 and 0.077, respectively. For the 2000 rpm runs, the above flow rates correspond to flow coefficients ϕ of 0.0, 0.013, 0.026, and 0.039, respectively. The above flow coefficients cover the range of typical leakage rates for the new Space Shuttle Alternate Turbopump (ATP) presently being developed. For the 1000 rpm runs, tests are performed for whirl frequency ratios in the range $-0.9 \leq \Omega/\omega \leq +0.9$ at 0.1 increments. For the 2000 rpm runs, tests are performed for whirl frequency ratios in the range $-0.6 \leq \Omega/\omega \leq +0.7$ at 0.1 increments. Tests with the swirl vane installed are conducted at a shaft speed of 2000 rpm and the same flow rates as above. With the swirl vane, the above leakage flow rates yield swirl ratios Γ of 0.0, 0.5, 1.0, and 1.5, respectively. The above test matrix is summarized in Tables 1 and 2.

Results for Tests Without Leakage Inlet Swirl

Figures 4 and 5 show plots of the dimensionless rotordynamic coefficients for 2000 and 1000 rpm, respectively for the three different number of brake ribs. Figures 6 and 7 show the whirl ratio. Tests are done at two different rotor speeds to access the Reynolds number effects. The 2000 rpm runs are shown first since they give the results at a lower flow coefficient range.
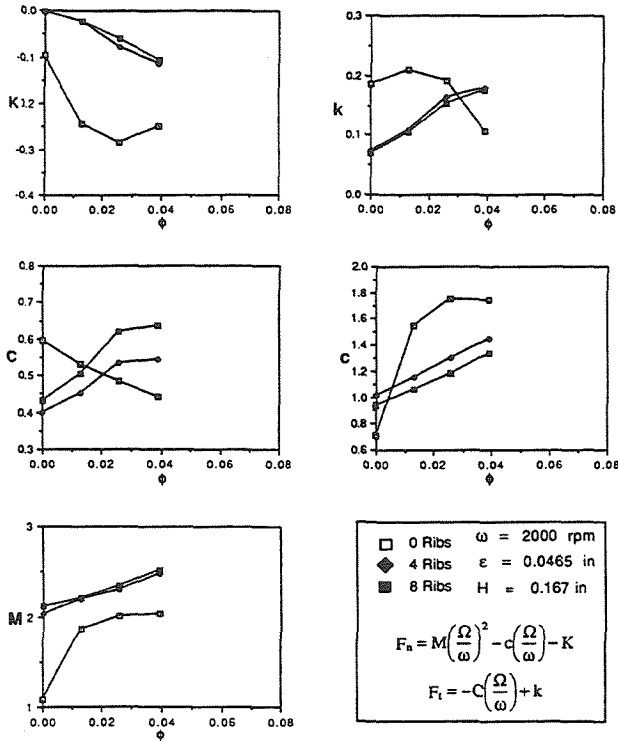
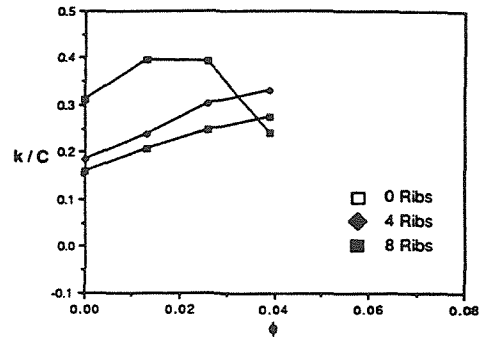Fig. 4 Rotordynamic coefficients at 2000 rpm, no swirl
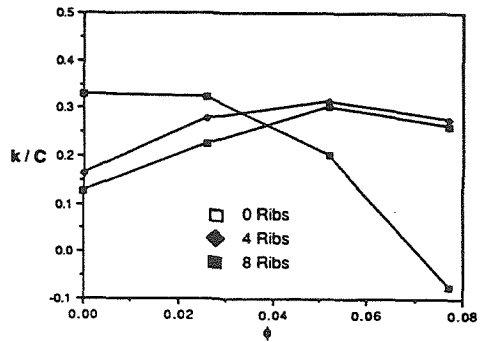

Fig. 6 Whirl ratio at 2000 rpm, no swirl

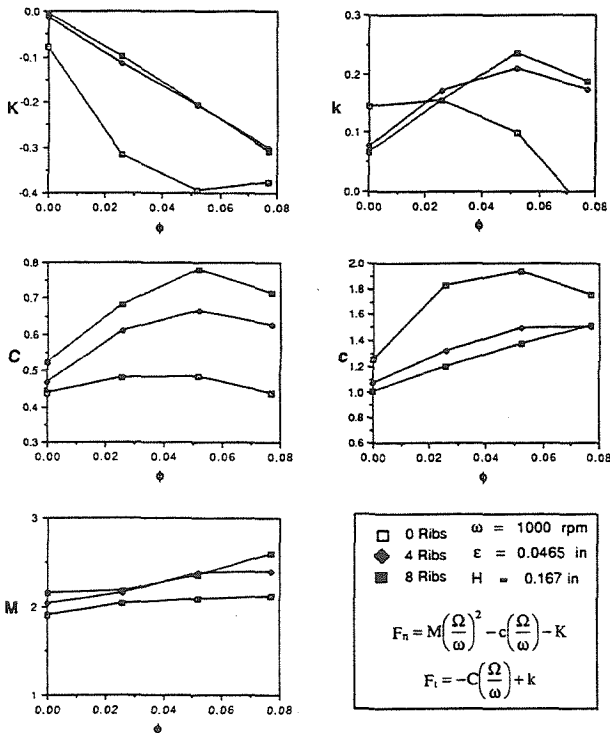Fig. 7 Whirl ratio at 1000 rpm, no swirl

Fig. 5 Rotordynamic coefficients at 1000 rpm, no swirl

A comparison of Figs. 4 and 5 show differences between corresponding coefficient plots at the lower flow coefficients indicating that Reynolds number effects are important at low flow rates. At flow coefficients above about 0.03 there seems to be little difference between corresponding coefficient plots at 1000

and 2000 rpm. Reynolds number effects are stronger with no brake ribs installed. C and k seem to have the greatest discrepancies between the 1000 and 2000 rpm runs.

Focusing on the coefficients corresponding to the tangential force, we can see that with no brakes the tangential force decreases with increasing leakage flow rate, as was found previously by Guinzburg (1992a). The cross-coupled stiffness coefficient, k, is decreased by increasing the flow from 0 to 30 GPM, and for the 1000 rpm case, C remains essentially constant. Hence the range for which the tangential force is destabilizing, k/C, decreases with increasing flow rate. This can be seen in Fig. 7. However, looking at k for the case with 4 or 8 brake ribs, the opposite trend with flow rate is observed. The cross-coupled stiffness increases as the flow rate increases from 0 to 30 GPM in both the 1000 and 2000 rpm runs. The above may appear to indicate that brakes are not beneficial. On the contrary, although the destabilizing tangential force with brakes increases with flow rate, there is a flow rate below which the tangential force with brakes is less than the tangential force without brakes. From the k plots in Fig. 4 and 5 we can see that below $\phi = 0.025$ the cross-coupled stiffness coefficient is reduced by the addition of 4 or 8 brakes. 8 brakes are only marginally more effective than 4. The beneficial effect of brakes is better exemplified by looking at the whirl ratio plots in Figs. 6 and 7. Below about $\phi = 0.03$, the range of destabilizing tangential force is much less with the addition of brakes.

Focusing on the coefficients corresponding to the normal force, we can see that with no brakes, the normal force increases with increasing leakage flow rate. K becomes more negative with increasing flow, hence increasing the normal force at zero whirl frequency and therefore is destabilizing. The same is true with 4 or 8 brakes, but we can also see from K that the destabilizing normal force is significantly reduced by the addition of brakes throughout the range of flow rates tested.
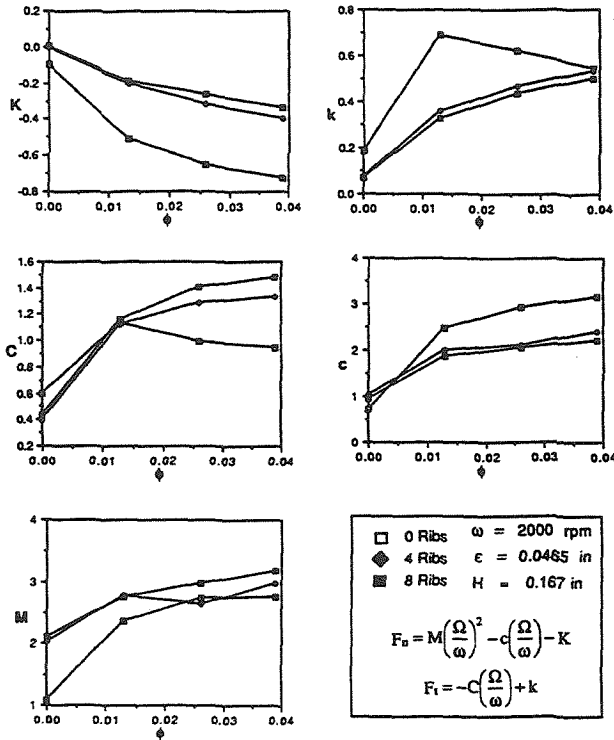
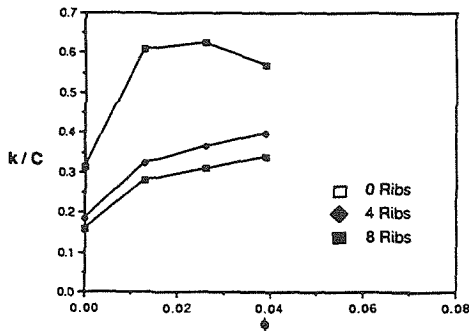**Fig. 8 Rotordynamic coefficients at 2000 rpm with swirl**

$$F_n = M\left(\frac{\Omega}{\omega}\right)^2 - c\left(\frac{\Omega}{\omega}\right) - K$$

$$F_t = -C\left(\frac{\Omega}{\omega}\right) + k$$

$\omega = 2000$ rpm
$\epsilon = 0.0465$ in
$H = 0.167$ in

□ 0 Ribs
◆ 4 Ribs
■ 8 Ribs

Fig. 9 Whirl ratio at 2000 rpm with swirl

□ 0 Ribs
◆ 4 Ribs
■ 8 Ribs

ratio. But, for the entire flow range tested, the cross-coupled stiffness is decreased by the addition of brakes.

Focusing on the coefficient K corresponding to the normal force, K is much large in the presence of swirl. We can see that with no brakes the normal force increases with increasing leakage flow rate. The same is true with 4 or 8 brakes, although from K, the destabilizing normal force is significantly reduced by the addition of brakes throughout the range of flow rates tested.

The most dramatic beneficial effect of brakes is found by comparing the whirl ratio plots for 4 or 8 brakes without and with swirl, Figs. 6 and 9, respectively. The 4 or 8 brake runs with and without swirl are almost identical. This indicates that the brakes almost completely eliminated the effect of swirl. With brakes present, swirl produces only a slight increase in the range for which the tangential force is destabilizing. Also, looking at Fig. 9, for all flow rates tested, the addition of brakes reduces the range for which the tangential force is destabilizing.

Conclusions

The influence of swirl brakes on the rotordynamic forces generated by discharge-to-suction leakage flows in centrifugal pumps with and without leakage inlet swirl has been investigated. The destabilizing normal force at zero whirl is reduced by the addition of brakes. The tangential force and the range of whirl frequency ratios for which the tangential force is destabilizing is reduced by the addition of brakes for low leakage flow rates. Brakes are beneficial in reducing the tangential force up to a higher leakage flow rate in the presence of leakage inlet swirl. Finally, the increase in the range of whirl frequency ratios for which the tangential force is destabilizing due to an increase in the leakage inlet swirl is nearly eliminated by the addition of swirl brakes.

Acknowledgments

Results for Tests With Leakage Inlet Swirl

Figure 8 shows plots of the dimensionless rotordynamic coefficients for the 2000 rpm runs with leakage inlet swirl for the three different number of ribs. Figure 9 shows the whirl ratio. As was previously found by Guinzburg (1992b), swirl dramatically increases the tangential force. This is evident by comparing the plot of k without swirl from Fig. 4 with the plot of k with swirl from Fig. 8. Once again, with no brakes, it can be seen that as the leakage rate increases, the tangential forces decrease, even though in the process the swirl ratio is increased. The stabilizing effect of an increase in flow rate dominates the destabilizing effect of an increase in swirl ratio. When 4 or 8 brake ribs are used, the opposite trend with flow rate is observed, as shown with the results without swirl. With brakes, the tangential force increases with flow rate and swirl

References

Adkins, D. R. and Brennen, C. E., 1988, "Analysis of Hydrodynamic Radial Forces on Centrifugal Pump Impellers," ASME JOURNAL OF FLUIDS ENGINEERING, Vol. 110, No. 1, pp. 20–28.

Childs, D. W., Baskharone, E., and Ramsey, C., 1990, "Test Results for Rotordynamic Coefficients of the SSME HPOTP Turbine Interstage Seal with Two Swirl Brakes," ASME, Journal of Tribology, 90-Trib-45.

Franz, R. J., 1989, "Experimental Investigation of the Effect of Cavitation on the Rotordynamic Forces on a Whirling Centrifugal Pump Impeller," Ph.D. thesis, California Institute of Technology.

Guinzburg, A., 1992a, "Rotordynamic Forces Generated By Discharge-To-Suction Leakage Flows in Centrifugal Pumps," Ph.D. thesis, California Institute of Technology.

Guinzburg, A., 1992b, "The Effect of Inlet Swirl on the Rotordynamic Shroud Forces in a Centrifugal Pump," ASME Paper 92-GT-126.

Jery, B., 1986, "Experimental Study of Unsteady Hydrodynamic Force Matrices on Whirling Centrifugal Pump Impellers," Ph.D. thesis, California Institute of Technology.

Zhuang, F., 1989, "Experimental Investigation of the Hydrodynamic Forces on the Shroud of a Centrifugal Pump Impeller," E249.9, Division of Engineering and Applied Science, California Institute of Technology.

TRANSACTIONS OF THE ASME

JOURNAL OF FLUIDS ENGINEERING

Chapter 4

Influence of Injectant Mach Number and Temperature on Supersonic Film Cooling

Influence of Injectant Mach Number and Temperature on Supersonic Film Cooling

K. A. Juhany,* M. L. Hunt,† and J. M. Sivo‡
California Institute of Technology, Pasadena, California 91125

The current work is an experimental investigation of the dependence of film cooling effectiveness on the injection Mach number, velocity, and mass flux. The freestream Mach number is 2.4, and the injection Mach numbers range from 1.2 to 2.2 for both air and helium injection. The adiabatic wall temperature is measured directly. The injection velocity and mass flux are varied by changing the total temperature and Mach number while maintaining matched pressure conditions between the injected flow and that of the freestream. The total temperature of the freestream is 295 K, and for the injection it ranges from 215–390 K. The results indicate an increase in film cooling effectiveness as the injection rate is increased. With the exception of heated helium runs, larger injection Mach numbers slightly increase the effective cooling length per mass injection rate. The results for helium injection indicate an increase in effectiveness as compared to that for air injection. Heated injection, with the injectant to freestream velocity ratios greater than 1, exhibit a rise in wall temperature downstream of the slot resulting in effectiveness values greater than 1. The experimental results are also compared with earlier studies in the literature.

Nomenclature

h_t = total enthalpy
M = Mach number
Re = Reynolds number
r = velocity ratio, u_i/u_∞
s = slot height
T_i = injection temperature
T_r = recovery temperature
T_t = total temperature
T_w = wall temperature
u_i = injection velocity
u_∞ = freestream velocity
X_{cl} = cooling length
x = streamwise distance
δ = boundary-layer thickness
η = film cooling effectiveness
λ = mass flux ratio, $\rho_i u_i/\rho_\infty u_\infty$
ν = kinematic viscosity
ρ = density

Introduction

NEW designs of supersonic and hypersonic vehicles have brought renewed interest in the areas of aerodynamic heating and active cooling techniques. One of the limiting design parameters for these vehicles is the maximum temperature and heat flux that is sustainable by the vehicle exterior and engine interior. For example, the afterburner temperature in an engine flying at Mach 5 is expected to exceed 2000 K.[1] An estimate of heating to the propulsion system is 10 kW/cm² with peak values upward of 50 kW/cm².[2] Although new materials and designs that integrate the propulsion system with the airframe are being introduced to account for the high temperatures and heat fluxes, the vehicles must also rely on active cooling techniques.

One proposed cooling method for supersonic or hypersonic flight is tangential slot injection or film cooling. Film cooling is a widely used technique to protect aircraft structures, rocket nozzles,[3] plug nozzles,[4] and turbine blades[5] from high-temperature environments. A thin layer or film of low-temperature gas is injected along the surface, in the direction parallel to the freestream. As the film-coolant fluid mixes with the higher temperature mainstream, the temperature of the gas film increases, reducing the film-cooling effectiveness. Previous experimental studies on film cooling have been predominantly in the area of incompressible flow. In the area of compressible flow, extensive work on film cooling has been done in cooling jet engine turbine blades. These studies involve flows with velocities below sonic conditions. Few studies have examined supersonic film cooling, especially with variable Mach number injection. More data are needed with low molecular weight gas injection as would be applicable to the National Aero-Space Plane. Furthermore, the results from existing supersonic film cooling studies vary considerably and little work has been done to resolve the discrepancies or to explain the physical phenomenon that impacts the mixing between the freestream and the injectant.[2]

The film-cooling flowfield can be divided into three regions[6]: 1) an inviscid core region, 2) a wall jet region, and 3) a boundary-layer region. The inviscid core region, like a free jet, contains a viscous layer that emanates from the lip and ends when it meets the growing slot-flow boundary layer. In this region the wall temperature remains constant at the recovery value of the injectant flow. The wall jet region starts at the location where the viscous layer originating from the lip meets the slot flow boundary layer. In this region, the wall begins to be affected by the mixing between the freestream and injectant. Due to intense mixing in this region, the temperature starts approaching that of the freestream value. Further downstream, the wall jet flow relaxes to a boundary-layer flow. Thus, film cooling flow combines different types of familiar flows: a free-jet flow, a wake flow, a shear layer flow, and a boundary-layer flow. Consequently, the behavior of the wall temperature should exhibit differences in each region.

Table 1 Supersonic film cooling studies

Author	Fluid	M_∞	M_i	r	λ	P_i/P_∞
Goldstein et al.[11]	Air	3	≤ 1	≤ 0.5	0.1–0.41	≤ 1 and ≥ 1
	He	3	<1		0.01–0.02	<1
Cary and Hefner[12,13]	Air	6	1	0.29–0.35	0.03–1.6	≤ 1 and ≥ 1
Rouser and Ewen[14]	H$_2$	2.3	1.9	1.95	0.15–0.58	0.5–2.0
	N$_2$	2.3	1.9	0.54	0.47–2.2	0.5–2.0
Current	Air	2.44	1.2–1.9	0.57–1.1	0.38–0.77	1
	He	2.44	1.3–2.2	1.6–2.6	0.18–0.44	1

In incompressible flow, the film-cooling effectiveness is defined as

$$\eta = \frac{T_w - T_\infty}{T_i - T_\infty} \qquad (1)$$

where T_∞ is the freestream temperature. An effectiveness of one corresponds with a wall that remains at the injection temperature, and the axial distance over which this occurs is referred to as the effective X_{el}. The fluid is heated as a result of mixing with the main flow, and the effectiveness decreases with downstream distance.

Early work on film cooling[7] has shown that under certain conditions the value of the heat transfer coefficient with film cooling quickly approaches that of the undisturbed boundary-layer flow. The same conclusion can be obtained theoretically if the incompressible, constant property, energy equation is applied to the film cooling flow.[7] As a consequence, the value of the adiabatic wall temperature in Eq. (1) is often not obtained directly, but instead determined from measurements of the wall heat flux and from calculations of the boundary-layer heat transfer coefficient.

Film cooling in low-speed flows has been thoroughly investigated (as reviewed by Goldstein[8]). A common purpose of these investigations was to develop a correlation for effectiveness, as defined in Eq. (1). The effectiveness results are often plotted as a function of downstream x, divided by s, and by the ratio of coolant mass flux to that of the freestream λ, $x/(s\lambda)$ where $\lambda = \rho_i u_i / \rho_\infty u_\infty$. The dependence of η on $x/(s\lambda)$ is developed from integral models for air injection into an airstream.[8] The effect of foreign gas injection is incorporated in the integral analysis by including the specific heat ratios, and is usually presented as $x/(s\lambda)(c_{p\infty}/c_{pi})$.

For supersonic flow, the effectiveness is often defined by replacing the freestream temperature with the freestream recovery temperature $T_{r\infty}$

$$\eta = \frac{T_{rw} - T_{r\infty}}{T_{ri} - T_{r\infty}} \qquad (2)$$

where T_{rw} and T_{ri} are the recovery temperatures measured along the surface and the recovery temperature of the injected fluid under adiabatic conditions. To correlate the data in high-speed flow, previous studies attempted to use modified incompressible flow correlations.[8] However, these correlations were not successful in predicting experimental measurements. The extension of the incompressible results to supersonic flow is complicated by two issues that are characteristic of high-speed flows: 1) the strong coupling between the momentum and energy equation, and 2) the appearance of shock waves. As a consequence of the strong coupling between the momentum and energy equations, the thermal features of the flow are strongly influenced by the hydrodynamic aspects. Unlike incompressible flow, the heat transfer coefficient with injection is expected to be different than the value of the undisturbed boundary layer. Beckwith and Bushnell[9] and Banken et al.[10] showed that the heat transfer coefficient with injection can differ significantly from that without injection. Therefore, the adiabatic wall temperature in Eq. (2) should be determined directly and not be inferred from the heat flux.

Studies of film cooling in which the adiabatic wall temperatures were measured directly, include the works of Goldstein et al.,[11] Cary and Hefner,[12,13] Rousar and Ewen,[14] and Baryshev et al.[15] The work by Goldstein et al.[11] considered sonic and subsonic injection of air and helium into a Mach 3 freestream. Both the injectant and the freestream flows were laminar, and the boundary-layer thickness at the injection slot was smaller than the slot height of the injectant (δ/s from 0.18 to 0.4). Goldstein et al. defined their effectiveness by replacing $T_{r\infty}$ in Eq. (2) with the recovery temperature measured with the injection of fluid at the same total temperature as the freestream. The results demonstrated that sonic injection of air significantly increased the film cooling effectiveness over that for subsonic injection.[11] In addition, the helium results indicated that the higher heat capacity of the injected fluid further increased the effectiveness. However, the helium studies were only performed for subsonic injection Mach numbers. Table 1 summarizes the parameters for this study and for other comparable studies.

The work by Cary and Hefner[12,13] involved sonic air injection into the hypersonic flow at Mach 6, and the results showed further increases in effectiveness over the supersonic results by Goldstein et al. In these experiments the freestream flow was turbulent and the boundary-layer thickness at the injection nozzle was considerably larger than the slot height (δ/s from 4.6 to 32). Cary and Hefner's definition of effectiveness was based on the freestream stagnation temperature $T_{t\infty}$ instead of $T_{r\infty}$ defined in Eq. (2). The results indicated that the effectiveness increased with injection temperature.

Rousar and Ewen[14] injected both hydrogen and nitrogen at Mach 1.9 into an airflow at Mach 2.3. The boundary layer was turbulent, but its thickness was not given. The effective cooling lengths for air injection were less than those found in the studies by Goldstein et al.[11] and by Cary and Hefner,[12,13] which could be due to differences in the experimental conditions. For hydrogen injection, the effective cooling lengths were larger than for any of the air studies, and the decrease in effectiveness as a function of downstream distance was significantly less for hydrogen. The injection Mach number and temperature remained constant, while the mass flow rates were varied by changing the injection pressure, so that the injectant was either underexpanded, overexpanded, or at matched conditions. The resulting mass flux ratios were 0.15 $< \lambda <$ 0.58 for hydrogen, and 0.47 $< \lambda <$ 2.2 for air.

To compare the air and hydrogen results, Rousar and Ewen modified the effectiveness definition using the difference in enthalpies

$$\eta = \frac{h_{t\infty} - h_{tw}}{h_{t\infty} - h_{ti}} \qquad (3)$$

where $h_{t\infty}$ indicates the total enthalpy of the freestream and h_{tw} is the total enthalpy for the edge of the viscous sublayer for adiabatic conditions. This definition is useful in presenting results for dissimilar gas injections; however, the definition relies on models for the entrainment rate to determine h_{tw}.

In addition to these studies, several film-cooling studies have measured the wall heat flux by using the transient techniques.[16-21] The studies by Alzner and Zakkay,[16] Zakkay et al.,[17] and Parathasarathy et al.[18] used a transient thin wall technique, where the heat transfer is determined from the

rate of change of the surface temperatures. The heat transfer coefficient value was calculated using flat plate turbulent boundary-layer correlations for flow without injection. As indicated earlier, this indirect method of determining the adiabatic wall temperature and the film cooling effectiveness can lead to significant errors because the heat transfer coefficient with injection can differ significantly from values without fluid injection.

In recent hypersonic film-cooling effectiveness studies[19-21] the heat transfer was measured using thin film resistance thermometers in a shock tunnel. The surface heat flux was measured with and without fluid injection. The no-injection boundary-layer results were used to determine the heat transfer coefficient. These boundary-layer heat transfer coefficients were then used with results of the injection experiments to calculate the film cooling effectiveness. Although, the measurement of heat flux was direct, and therefore more accurate than the studies of Refs. 16-18, obtaining the adiabatic wall temperature with injection by using the heat transfer coefficient without injection results in inaccuracies.

The approach in this experiment is to obtain the adiabatic wall temperature directly by insulating the wall. The data are compared to studies of Goldstein et al.,[11] Cary and Hefner,[12,13] and Rousar and Ewen[14] in which the adiabatic wall temperatures were measured directly.

Experimental Facility

In the current experiment, air and helium were used as the injectants, and the injection Mach number varied from $M_i = 1.2$ to $M_i = 2.2$. The mass flow rates were varied by controlling the injection temperature, injection Mach number, and matching the injection exit pressure to that of the freestream. The ranges of parameters for the present experiments are listed in Table 2.

The experiments were conducted in the Graduate Aeronautical Laboratory, California Institute of Technology (GALCIT) continuous supersonic wind tunnel. Figure 1 shows a schematic of half-nozzle configuration used in the slot injection experiments. Air entered the wind tunnel at ambient

Table 2   Experimental parameters

Injectant	$T_{ii}/T_{r\infty}$	M_i	U_i/U_∞	$\rho_i U_i/\rho_\infty U_\infty$
Air	1.13	1.3	0.72	0.38
	1.13	1.5	0.82	0.50
	1.13	1.8	0.91	0.61
	1.14	2.2	1.0	0.82
	1.32	2.2	1.1	0.77
	0.80	1.2	0.57	0.40
	0.76	1.5	0.66	0.59
	0.76	1.8	0.73	0.74
Helium	1.16	1.3	2.0	0.18
	1.16	1.6	2.2	0.23
	1.16	1.9	2.4	0.30
	1.24	2.2	2.6	0.34
	0.75	1.3	1.6	0.20
	0.71	1.9	1.9	0.44

Fig. 1   Schematic of wind-tunnel test section. Drawing not to scale.
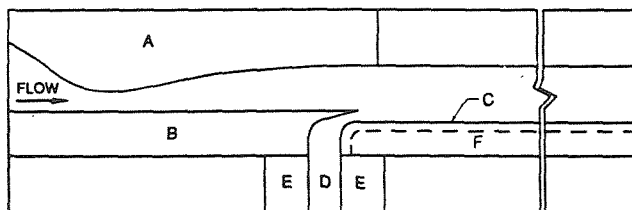
A - SUPERSONIC NOZZLE BLOCK
B - SLIDING INJECTION BLOCK
C - ADIABATIC WALL
D - INJECTANT SETTLING CHAMBER
E - INSULATING BLOCKS
F - LOW PRESSURE REGION

pressure (≈ 0.97 atm) and temperature ($\approx 28°C$). At the beginning of the test rhombus where the injectant slot was located, the boundary layer was turbulent with a thickness of 3.4 mm and a Re/m of 9.0×10^6. The nominal freestream Mach number was 2.44 ± 0.02. The total test section length and height were 400 and 25.4 mm, and the slot height at the exit of the injection nozzle was 1.5 mm.

The 2-mm-thick instrumented plate was made from Hastelloy-X®, a low thermal conductivity nickel-cobol alloy used to reduce conduction from the injection slot to the downstream section and from the plate sides. To minimize heat transfer from the instrumented plate to the exterior, the region behind the plate was open to the low-pressure downstream environment. Fifty-nine thermocouples were mounted on the back side of the plate. The thermocouples were epoxied into 1-mm holes, laser-drilled 0.3 mm below the surface. The plate also contained 48 pressure taps of which only 25 were connected for this experiment. The pressure taps were connected to piezoelectric transducers. The thermocouples and pressure taps were arranged in a diagonal fashion in the central third of the plate to provide concentrated measurements of pressure and temperature without interference. The diagonal arrangement made it possible to assess any heat exchange through the sides of the plate to the environment. All thermocouples and pressure transducers were connected to a PC-based data acquisition system. The wind tunnel was also equipped with a combined continuous and 10-ns spark source schlieren system for flow visualization.

The injectant gas was supplied from compressed gas bottles that were connected to a manifold and a pressure regulator. The regulator was used to adjust the pressure of the injectant before entering the turbine flow meter. Using the flow meter, the uncertainty in the mass flow measurements was approximately 5%, with the largest values occurring at the highest flow rates. After metering the flow, the injectant entered a heat exchanger that was used to increase or decrease the injectant temperature. For heated runs, the total temperature was increased to approximately 70°C using resistance tape heaters that were controlled with a variable voltage regulator. A few tests were made at a higher temperature (<120°C) to indicate the effect of further heating. Additional heating of the injectant would have resulted in an unfavorable heat conduction to the freestream boundary layer through the injectant-nozzle lip. For cooled runs, a dry-ice/alcohol mixture was used to decrease the injectant temperature to approximately −60°C. After exiting the heat exchanger, the flow was throttled to the injection reservoir where the total and static pressures, and the total temperature were measured. The total pressure was measured using a tube that faced the direction of the flow while the static pressure was measured at the wall; the difference between the two measurements were small, indicating that the flow was stagnant. To reduce conduction upstream to the primary flow, the injection reservoir was made from a wooden block.

Figure 2 shows the sliding block injection nozzle. The end of the sliding block was tapered to an angle of 10 deg which was used to form the injection nozzle. The lip thickness in this study was difficult to define since the lip had a wedge shape with a sharp trailing edge (0.25-mm thick). By moving the sliding block, the Mach number was varied by changing the height of nozzle throat. The termination of the nozzle at 10 deg resulted in a radial-type flow, similar to that of rocket nozzles, so that the flow out of the nozzle was not parallel to
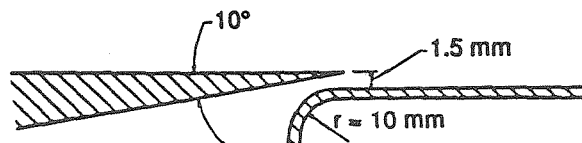

Fig. 2   Injection nozzle geometry.

the freestream flow. The effect of the injectant radial flow on the flow just downstream of the nozzle is discussed in the next section.

The injection Mach number reported in the study was determined from the height of the nozzle exit (1.5 mm) assuming zero displacement thickness, and by measuring the total temperature, total pressure, and mass flow rate of the injected gas. This method of calculating the Mach number agreed with the Mach number measured with the pitot probe at the center of the slot exit ($M \pm 0.1$) for Mach numbers 1.5 and higher.[22] However, the accuracy for the transonic Mach number injections range (≤ 1.2) was within $M \pm 0.2$, with Mach numbers always greater than unity. The calculation assumed a zero displacement thickness through the nozzle. The agreement between the calculation method and the pitot probe measurement indicated that the displacement thickness was small. A static pressure tap was also located within the nozzle, and this tap was used to verify that the flow within the nozzle was supersonic. The pressure tap located nearest to the slot was also checked to verify that the pressure was near matched conditions.

Experimental Results

Preliminary experiments were made to assess the effect of heat conduction between the environment and the test section, and to examine the impact of the backward facing step formed by the slot and the instrumented plate. As indicated by the thermocouples located nearer to the side walls of the test section, some heat conduction occurred along the edge of the plate. Without fluid injection, the adiabatic wall temperatures were at most 8°C higher than the value predicted assuming a turbulent recovery factor of 0.89 and using the total temperature of the freestream. The variation of the wall temperature from the expected adiabatic wall temperature without injection resulted from several factors: the upstream history effect on the boundary layer, the impingement of the step shock wave on the plate, and conduction. As observed in the schlieren system and through the static pressure taps, this shock was reflected several times within the test section. The temperatures measured near the sidewall of the tunnel were close to the temperature located at the center of the plate (less than 1°C), indicating low conduction along the sides of the plate. The plate responded quickly to temperature variations, but the wind-tunnel glass windows and the wooden injectant reservoir slowly reached thermal equilibrium. In all runs, sufficient time was given for the plate and the injectant reservoir to reach thermal equilibrium, usually 15 min. Correcting the effectiveness for conduction proved to be difficult because the heat transfer coefficient with injection is unknown.

The flow parameters for the 10 different experiments are listed in Table 2. The air experiments are for Mach numbers between 1.2–2.2, mass flux ratios between $0.38 \leq \lambda \leq 0.82$, and velocity ratios between $0.57 \leq r \leq 1.1$. The helium experiments are for Mach numbers from 1.2 to 2.2, mass flux ratios between $0.2 \leq \lambda \leq 0.44$, and velocity ratios between $1.6 \leq r \leq 2.6$. The definition of effectiveness for the presentation of the experimental results corresponds to the definition in Eq. (2), where $T_{r\infty}$ is the measured adiabatic wall temperature without fluid injection. The value of T_{ri} is the wall temperature measured just downstream of the injection nozzle. Using the measured values of $T_{r\infty}$ and T_{ri}, rather than the calculated values, gives a more accurate value of effectiveness.

Flow visualization studies using the schlieren optics were undertaken to investigate the flow downstream of the slot. The nozzle was set to an injectant Mach number, then the injection mass flow rate was increased until its value reached the matched pressure condition. As the injectant flow rate was increased towards the matched pressure value, a similar shock structure to the studies of Goldstein et al.[11] was observed. Figure 3 is a schlieren photograph of a Mach 2.2 slot
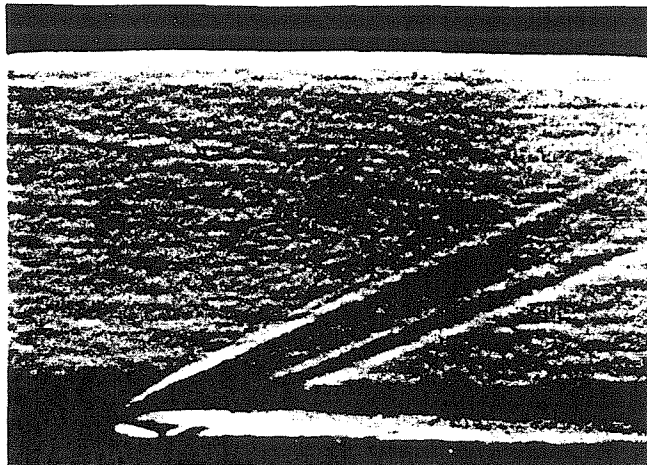

Fig. 3 Schlieren photograph of $M_i = 2.2$ air injection.

flow, which is a typical flow pattern for all the other injectant Mach numbers. The knife edge for the schlieren photograph is positioned parallel to the flow direction. The schlieren photograph shows the freestream boundary layer interacting with the injectant. The injectant is the bright region next to the wall, while the freestream boundary layer is the dark region just above the injectant. The injectant at the point of interaction is at an angle of 10 deg, with respect to the parallel free-stream. Although the injectant and the freestream are at matched pressure, a shock wave in both the freestream and injectant sides is produced to adjust the flow to the same orientation angle. The slot flow radial velocity is reduced as the wall is approached on the injectant side. The interaction between the freestream and the injectant flow starts at the slot tip. The disturbance due to the interaction is propagated through the Mach lines. The streamlines closer to the wall feel the disturbance at a larger axial distance from the slot exit than streamlines farther from the wall. Consequently, the streamlines closer to the wall expand more than ones farther away from the wall, increasing in Mach number and decreasing in pressure. Therefore, the shock wave, produced in the injectant flow, increases in strength as it approaches the wall. The injectant shock wave interacts with the laminar boundary layer, resulting in separation, but reattachment soon follows because the boundary layer is small and the strength of the shock wave appears to be close to the incipient value. The above information concerning the shock structure out of the slot was examined computationally,[23] using the MUSCL scheme developed by Lappas.[24] It was found that the shock wave strength in the injectant flow, measured in terms of static pressure rise, ranged from 1.1 to 1.3 for the lowest and highest injection Mach number, respectively. The leading separation shock, the expansion wave, and the recompression shock (characteristic of shock wave boundary-layer separation) are indicated by two sharp bright lines surrounding a dark region (expansion wave). The effect of weak shock waves on the adiabatic wall temperature is not significant,[22] especially next to the slot. Previous results[17] indicate that the slot-flow lip shock wave does not seriously degrade film cooling effectiveness.

The addition of mass by injection in the fixed test section area resulted in a pressure increase that was proportional to the injection rate. Figure 4 shows a selection of wall pressure distributions for some of the tests. The pressure distribution along the wall indicates that the pressures for most runs are nearly constant for the first 60 slot heights, but gradually the pressure begins to increase. The highest pressure increase is from 6.2 kPa near the injection slot to 9.6 kPa at $X/s = 300$ for the $\lambda = 0.74$ case. The spikes in the pressure profile are a result of the lip shocks propagating through the test section and impinging on the wall. Although the shock waves in the tunnel are weak, their signature on the wall indicates the
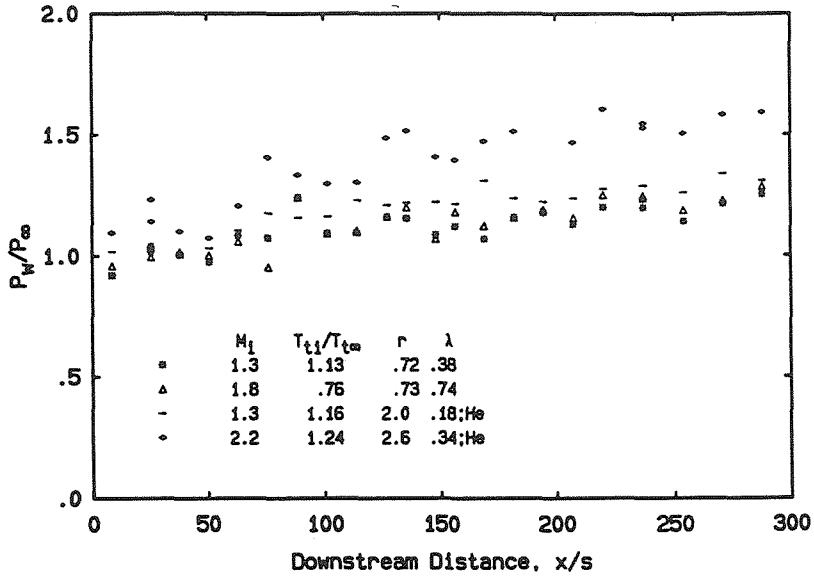
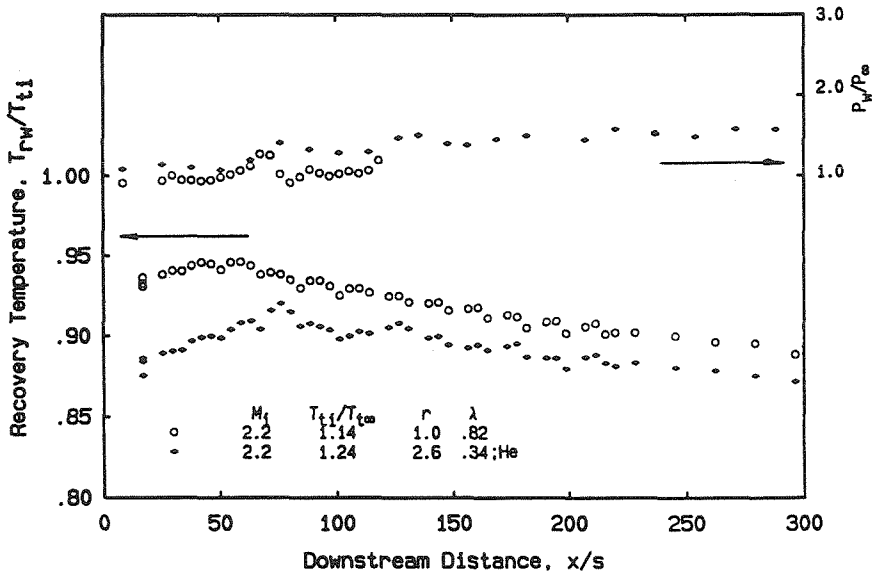Fig. 4 Wall static pressure distribution for air and helium injection.

Fig. 5 Temperature and pressure ratios of heated helium and air injections displaying an increase in temperature downstream of the slot. The upper data set are the pressure ratio, while the lower ones are the temperature ratio.

added effect of the reflected shock. In previous low-speed film cooling experiments, it was found that pressure gradients of the magnitude experienced under the current experimental conditions did not influence the film cooling effectiveness,[8] while the effect of pressure gradient in supersonic flow (not associated with shock waves) is not well documented. The comparisons in this study are based on the assumption that the pressure gradients of the magnitude experienced in the current experiments have little effect on the film cooling effectiveness.

As discussed earlier, a typical plot of temperature with heated injection vs distance downstream of the slot shows the temperature near the slot to be constant for a short distance in the inviscid core region. Then the temperature drops as the freestream mixes with the injectant. The opposite trend occurs when a cold injectant is used. In general, for both heated and cooled injection, the effectiveness value follows the same temperature trend. However, for heated injection at high velocities ($r \geq 1$), there is a distance downstream of the slot where the recovery temperature increases at constant pressure, even beyond the temperature T_{ri}. This increase in temperature results in an increase in effectiveness with downstream distance to values above 1, as defined by Eq. (2). This

phenomenon is demonstrated in Fig. 5, which shows results of temperature normalized by the injectant stagnation temperature, and pressure normalized by the freestream pressure for Mach 2.2 heated injection of air and helium. The length in which this rise occurs is shown to extend to 45 slot heights in the case of air, and 70 slot heights in the case of helium. The increase in temperature is a result of the flow near the wall, composed of mostly injectant fluid, slowing down due to the mixing process between the freestream and the injectant.[22] Additional heating would also occur when the injectant boundary layer transitions from a laminar to a turbulent boundary layer. This rise in temperature should also occur with cold injection, but the effect is not noticeable since the temperature also rises due to the mixing with the hotter freestream.

Figures 6–9 show the film cooling effectiveness as a function of downstream distance divided by slot height x/s. Data above $\eta > 1$ is not shown, but it occurs for all heated injection whose r is greater than 1. The highest effectiveness values obtained in the cases of data sets shown in Fig. 5 are 1.2 and 1.5 for air and helium injection, respectively. As indicated in the figures, X_{cl} ranges from approximately 30 to 300 slot heights depending on the fluid, the injection rate, and the Mach num-
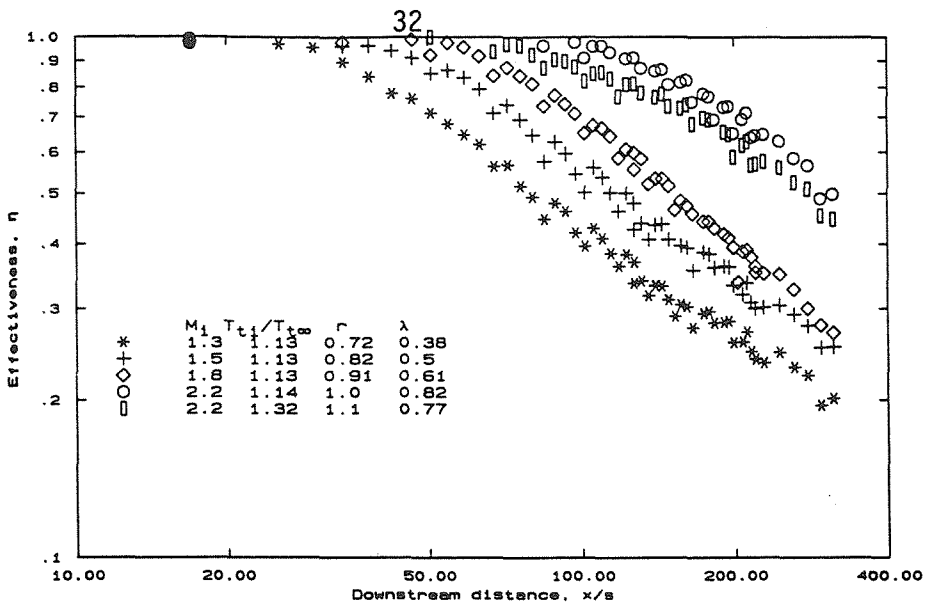
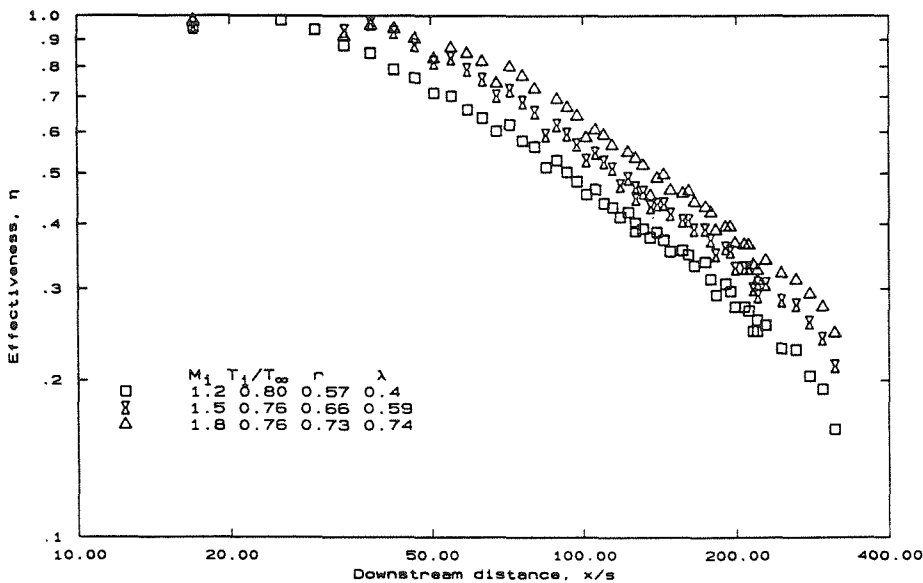Fig. 6 Heated air injection, η as a function of x/s.

Fig. 7 Cooled air injection, η as a function of x/s.

ber. The decrease in effectiveness downstream of X_{cl} also appears to depend on these parameters.

In Fig. 6 the results are presented for heated air injection ($T_t \approx 70°C$). For a fixed injectant temperature, increasing the injectant Mach number raises both the velocity ratio and mass flux ratio which results in an increased cooling length. By comparing the results for $M_i = 1.3$ and $M_i = 1.8$, the increase in cooling length is approximately $30s$, but requires a 60% increase in mass flux. When increasing the injection Mach number to 2.2, corresponding to a velocity ratio of unity, the rate of decay of effectiveness is reduced compared to other Mach number injections. Additional heating of the Mach 2.2 injection to a value of $T_{ti}/T_{t\infty} = 1.32$ results in a 10% increase in velocity and a 6% reduction in mass flow rate, but only results in a small change in effectiveness. Figure 7 shows results for cooled air injection ($T_t \approx -40°C$). For cooled injection, the results for $M_i = 1.8$ indicates only a slight increase in cooling length beyond the results for $M_i = 1.5$. When the Mach number is increased to 1.8 in both cases of heated and cooled injections, the improvement in effectiveness is less in the case of cooled injection, whose increase in λ is even higher than that for the heated injection.

Figure 8 shows the results of effectiveness with heated helium injection. The results show a large change in effectiveness when the injection Mach number is increased from 1.3 to 1.6. High effectiveness values (greater than 0.8) are achieved for the entire test length of 300 slot heights, when the injection Mach number is more than 1.6. Figure 8 also shows that effectiveness does not improve beyond the Mach 1.9 value, corresponding to a velocity ratio of $r = 2.4$. The injectant of Mach 2.2 is at a higher temperature and produces similar effectiveness values to the Mach 1.9 case. Figure 9 presents the measurements for the cooled helium injection studies. The results show an increase in cooling length of approximately $20s$ for a 120% increase in the fluid injection rate. The cooled helium injection produces cooling lengths much smaller than that produced by the heated helium injection. In contrast to air injection, increasing the helium velocity ratio beyond 1, $r > 1$, increases the effectiveness until the value of $r = 2.4$ is reached.

Figure 10 presents the effectiveness results for all of the experimental runs as a function of $x/(s\lambda)(c_{p\infty}/c_{pi})$, which is the parameter suggested by the integral analyses.[8] As shown in the figure, the parameter $x/(s\lambda)(c_{p\infty}/c_{pi})$ nearly collapses all
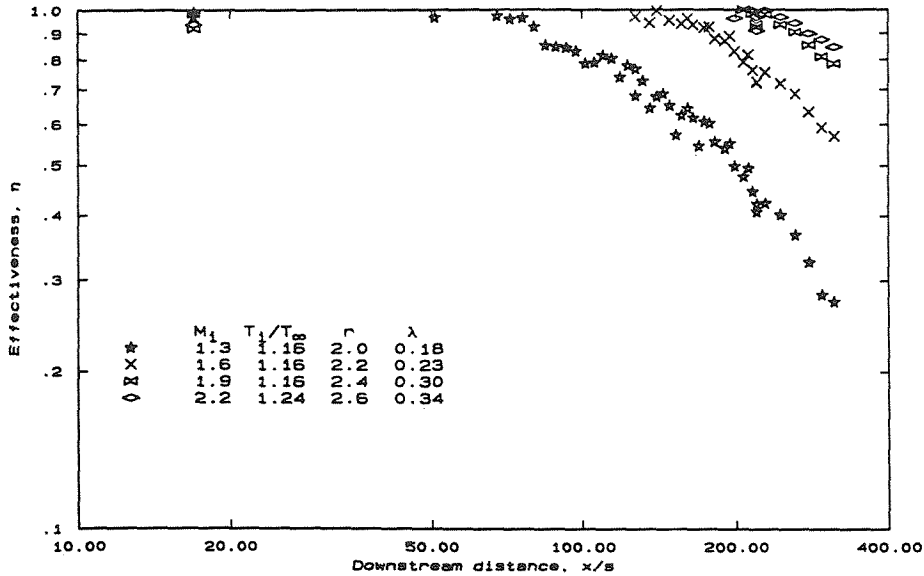

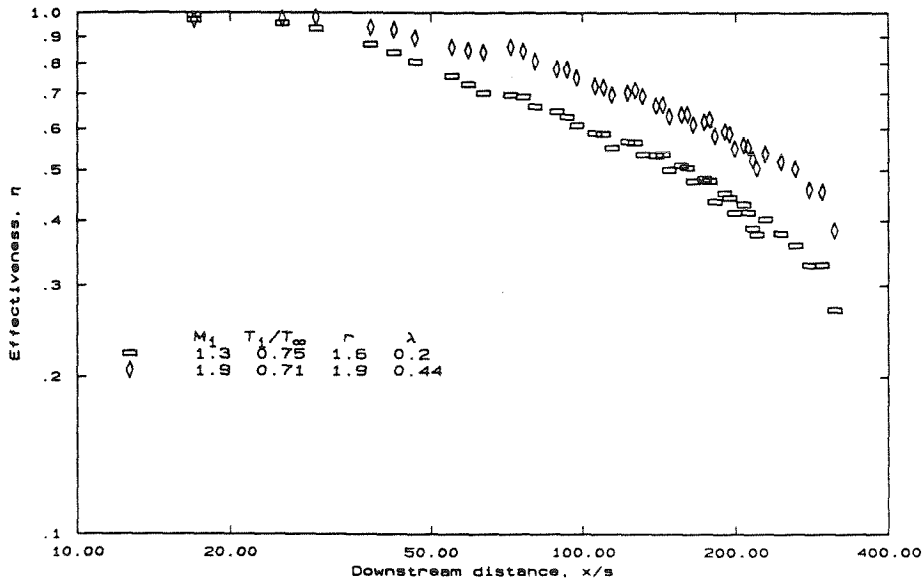Fig. 8 Heated helium injection, η as a function of x/s.

Fig. 9 Cooled helium injection, η as a function of x/s.

the data, with the exception of the cooled helium injection. Figure 10 indicates that the cooling lengths per mass injection rate $X_{cl}/(s\lambda)$ are close for all the air runs, although it appears that the values are slightly larger for the heated air runs. The heated runs also decay at a higher rate than found in the cooled runs, especially for helium. It was shown earlier that there was an initial region where the temperature rose beyond the value at the exit of the slot (apparent in the case of heated injection with $r > 1$). The temperature rise results in higher effectiveness values for heated injection and lower ones for cooled injection. This temperature rise with downstream distance occurs more significantly for helium injection. Therefore, the difference between effectiveness values of the heated and cooled injection is expected to be more significant for helium. In addition to the physical phenomena of increased effectiveness with injectant temperature, higher values of effectiveness for a given $x/(s\lambda)(c_{p\infty}/c_{pi})$ also result from the assumptions made in the integral analysis. The integral analysis that produces the correlation parameter $x/(s\lambda)(c_{p\infty}/c_{pi})$ assumes that the adiabatic wall, $T_{rw}(x)$ in Eq. (2), is equal to the mass averaged temperature downstream of the slot.[8] The mass averaged temperature value is between the adiabatic wall temperature and that of the freestream. Using the adi-

abatic wall temperature instead of the mass averaged value results in an overestimate of η for heated injection and an underestimate of η for the cooled injection.

In Fig. 10, the experimental results are also compared with the experimental measurements by Goldstein et al.,[11] Cary and Hefner,[12,13] and Rouser and Ewen.[14] To compare these studies, the experimental curves of Cary and Hefner, and of Rouser and Ewen are recalculated from their figures to correspond with the effectiveness definition used in the present work. Also, the curves corresponding to experimental results of Cary and Hefner in Fig. 10 represents bounds of their data. Except for the results of cooled helium injections and that of Rouser and Ewen, the experiments show similar values of the cooling length parameter $X_{cl}/(s\lambda)(c_{p\infty}/c_{pi})$. Beyond $X_{cl}/(s\lambda)(c_{p\infty}/c_{pi})$, the drop in effectiveness is smallest for the hydrogen injection studies by Rouser and Ewen,[14] followed by the results for sonic air injection into a hypersonic freestream by Cary and Hefner.[12,13] The drop in effectiveness of the current experiment is larger than that of Cary and Hefner.[12,13] The difference may be attributed to slower mixing in hypersonic flow boundary layers as compared to the mixing in the current supersonic flow results. The Goldstein et al.[11] results are for a similar Mach number as the present experiments. However,
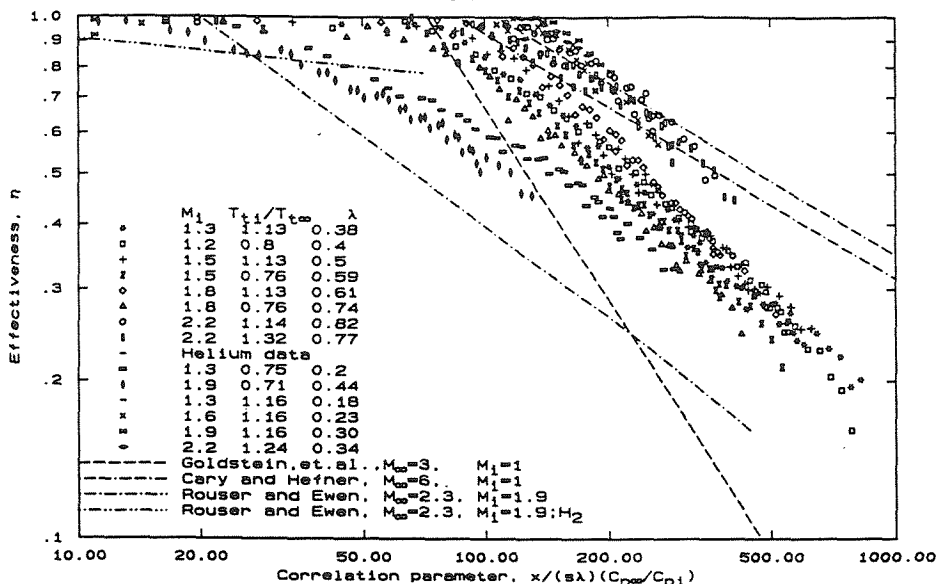
Fig. 10 Comparison of experimental results with previous data using the correlation parameter.
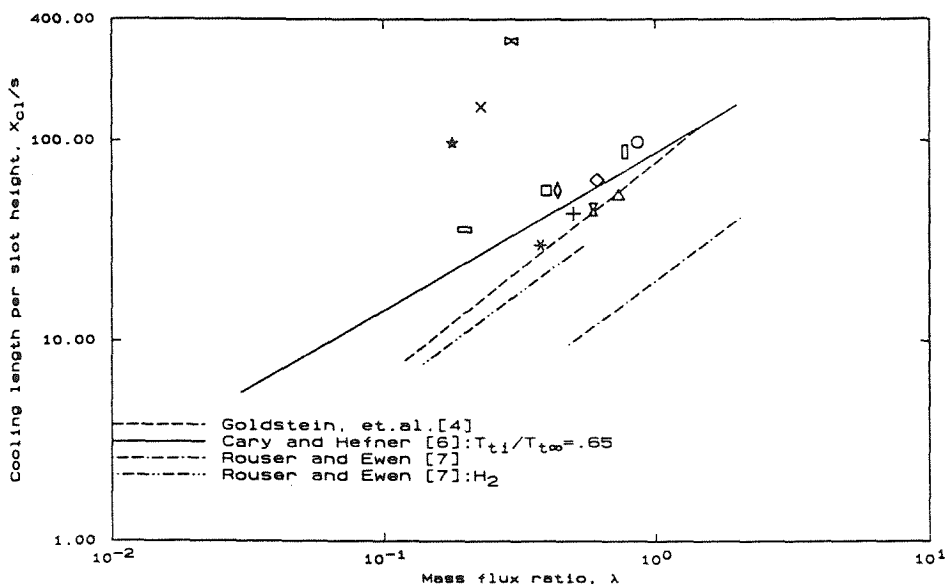

Fig. 11 Symbols correspond to the ones in Fig. 10. X_{cl} as a function of the mass flux ratios.

their results indicate a much steeper decrease in effectiveness which may be due to the relatively large thickness of the nozzle lip as compared to the thickness of the boundary layer. Their geometry may induce a large wake that would enhance mixing between the injectant and the mainstream. The boundary layer to lip thickness ratio of 0.4 in Goldstein's study is small when compared to 6 and 39 of Ref. 25, and 22 and 2.14 of Ref. 19, whose finding was that lip thickness did not affect film cooling. The relatively low air results by Rouser and Ewen[14] are anomalous since the flow conditions are similar to that for the present experiments. Their hydrogen results, as compared with that for air or helium injection, do demonstrate the effect of the increasing the injectant heat capacity.

In several of the references,[4,20,21] other correlation parameters such as $x/(s\lambda^{0.8})$, $x/(s\lambda)Re_i^{-0.25}\nu_x/\nu_i$, and $x/(s\lambda)Re_i^{-0.25}(\nu_x/\nu_i)(\rho_i/\rho_x)^{0.4}[1 + 0.5(\gamma - 1)M_i^2]$ have been used to present the data. These parameters were tried, but the parameters did not indicate a better representation of the results than $x/(s\lambda)(c_{px}/c_{pi})$. Note that these parameters are based on the injection conditions as compared to those of the freestream; as a result these parameters merely shift the curves along the axes of the graph and do not change the slope of the curves.

As a further comparison of the experimental findings, Fig. 11 shows the cooling lengths for each of the experiments as a function of the mass flux ratios. The values of X_{cl} are determined by performing a least squares fit to the data points corresponding to $\eta < 0.80$, and extrapolating the curve to find the $x/(s\lambda)$ value in which $\eta = 1.0$. For the helium injection cases of $M_x = 1.9$ and $T_{ti}/T_{tx} = 1.16$, only the last point tested is near the value of 0.8, and therefore, the corresponding value of x/s is used. For the case of $M_x = 2.2$ and $T_{ti}/T_{tx} = 1.24$, all values are larger than 0.8, so its value of X_{cl}/s is not indicated in the figure. For the same injection rate, the helium results show a higher effectiveness than the corresponding air measurements which is due to the relatively high specific heat of helium as compared to that for air. The figure indicates that the heated helium runs clearly have the highest cooling lengths for a given injection rate. The figure shows that the cooling length increases with Mach number for a constant injection rate. The figure also suggests that except for the anomalous cooling run with $M_i = 1.2$, the heating experiments produced larger values of X_{cl}. The cooling lengths for cold helium injection are not significantly larger than the air results; however, as noted earlier the decrease in effectiveness downstream of X_{cl} occurred more slowly. The figure

again indicates the correspondence between the present cooling lengths and the results from Goldstein et al.[11] and Cary and Hefner.[12,13]

Conclusions

The current experiments examine supersonic film cooling effectiveness for air and helium injection. In the experiments, the static pressure between the freestream and the injectant were matched, and the total temperature and Mach number of the injectant were varied. The wall pressure and the wall temperature were measured. The adiabatic wall temperatures were measured directly by insulating the surface.

For heated injection of velocity ratio greater than 1, the temperature increased downstream of the slot, resulting in effectiveness greater than one. This rise is attributed to the deceleration of the injectant as it mixes with the freestream boundary layer and to the transition of the injectant boundary layer.

Generally, effectiveness improves with increasing the injectant Mach number. However, for the cold runs of helium and air, the change in Mach number produces a small change in effectiveness. For λ or r, varying the Mach number of air injection produces a small change in the cooling length per unit mass flux $X_{cl}/(s\lambda)$. In the case of helium injection, keeping λ constant and increasing the Mach number produces a higher cooling length. To vary the injectant Mach number while maintaining the same λ or r, involves changing the temperature. To attribute the increase in cooling length to Mach number alone is not conclusive since the behavior of heated and cooled injection is different. Comparison between helium and air experiments indicates that the effectiveness increases with the heat capacity of the gas.

High effectiveness values far downstream are found with the heated injections for velocity ratios greater than 1. Heated helium injections of velocity ratio greater than 2 produce effectiveness values greater than 0.8 for 300 slot heights downstream of injection point. The increase in temperature downstream of the slot could partly explain the high effectiveness values obtained in the cases of heated injections with $r > 1$.

Previous studies that directly obtained the adiabatic wall temperature are compared with the current experiment. The simple correlation parameter $x/(s\lambda)(c_{px}/c_{pi})$ is demonstrated to be the best choice for correlating the data. However, the cooled helium injection does not conform to this correlation.

References

[1]DeMeis, R., "Multimodes to Mach 5," *Aero—Space America*, Vol. 25, No. 9, 1987, pp. 50–53.

[2]Simoneau, R. J., Hendricks, R. C., and Gladden, H. J., "Heat Transfer in Aerospace Propulsion," *Proceedings of ASME National Heat Transfer Conference* (Houston, TX), Vol. 3, 1988, pp. 1–22.

[3]Lucas, J. G., and Golladay, R. L., "Gaseous-Film Cooling of a Rocket Motor with Injection Near the Throat," NASA TN D-3836, Feb. 1967.

[4]Nosek, S. M., and Straight, D. M., "Heat-Transfer Characteristics of Partially Film Cooled Plug Nozzle on A J-85 Afterburning Turbojet Engine," NASA TM X-3362, March 1976.

[5]Gladden, H. J., and Simoneau, R. J., "Review and Assessment of the Database and Numerical Modeling Turbine Heat Transfer," *Symposium Toward Improved Durability in Advanced Aircraft Engine Hot Sections* (Amsterdam, The Netherlands), edited by D. E. Sokolowski, ASME, 1988, pp. 39–56.

[6]Seban, R. A., and Back, L. H. "Velocity and Temperature Profiles in Turbulent Boundary Layer with Tangential Injection," *Journal of Heat Transfer*, Vol. 84, No. 1, 1962, pp. 45–54.

[7]Eckert, E. R. G., and Drake, M. R., Jr., *Analysis of Heat and Mass Transfer*, 2nd ed., McGraw-Hill, New York, 1972, pp. 455–458.

[8]Goldstein, R. J., "Film Cooling," *Advances in Heat Transfer*, Vol. 7, 1971, pp. 321–380.

[9]Beckwith, I. E., and Bushnell, D. M., "Calculation by a Finite-Difference Method of Supersonic Turbulent Boundary Layers with Tangential Slot Injection," NASA TN D-6221, April 1971.

[10]Banken, G. J., Roberts, D. W., Holcomb, J. E., and Birch, S. F., "An Investigation of Film Cooling on a Hypersonic Vehicle Using a P.N.S. Flow Analysis Code," AIAA Paper 85-1591, July 1985.

[11]Goldstein, R. J., Eckert, E. R. G., Tsou, F. K., and Haji-Sheikh, A., "Film Cooling with Air and Helium Injection Through a Rearward-Facing Slot into a Supersonic Air Flow," *AIAA Journal*, Vol. 4, No. 6, 1966, pp. 981–985.

[12]Cary, A. M., and Hefner, J. N., "Film Cooling Effectiveness in Hypersonic Turbulent Flow," *AIAA Journal*, Vol. 8, No. 11, 1970, pp. 2090, 2091.

[13]Cary, A. M., and Hefner, J. N., "Film-Cooling Effectiveness and Skin Friction in Hypersonic Turbulent Flow," *AIAA Journal*, Vol. 10, No. 9, 1972, pp. 1188–1193.

[14]Rousar, D. C., and Ewen, R. L., "Hydrogen Film Cooling Investigation," NASA CR 121235, Aug. 1973.

[15]Baryshev, Y. V., Leont'yev, A. I., and Rozhdestvenskiy, V. I., "Heat Transfer in the Zone of Interaction Between a Shock and the Boundary Layer," *Heat Transfer—Soviet Research*, Vol. 7, No. 6, 1975, pp. 19–23.

[16]Alzner, E., and Zakkay, V., "Turbulent Boundary Layer Shock Interaction with and Without Injection," *AIAA Journal*, Vol. 9, No. 9, 1971, pp. 1769–1776.

[17]Zakkay, V., Sakell, L., and Parthasarathy, K., "An Experimental Investigation of Supersonic Slot Cooling," *Proceedings of the 1970 Heat Transfer and Fluid Mechanics Institute*, edited by T. Sarpkaya, Stanford Univ. Press, Stanford, CA, 1970, pp. 88–103.

[18]Parthasarathy, K., and Zakkay, V., "An Experimental Investigation of Turbulent Slot Injection at Mach 6," *AIAA Journal*, Vol. 8, No. 7, 1970, pp. 1302–1307.

[19]Olsen, G. C., Nowak, R. J., Holden, M. S., and Baker, N. R., "Experimental Results for Film Cooling in 2-D Supersonic Flow Including Coolant Delivery Pressure, Geometry and Incident Shock Effects," AIAA Paper 90-0605, Jan. 1990.

[20]Holden, M. S., Nowak, R. J., Olsen, G. C., and Rodriguez, K. M., "Experimental Studies of Shock Wave/Wall Jet Interaction in Hypersonic Flow," AIAA Paper 90-0607, Jan. 1990.

[21]Majeski, J. A., and Weatherford, R. H., "Development of an Empirical Correlation for Film-Cooling Effectiveness," AIAA Paper 88-2624, June 1988.

[22]Juhany, K. A., and Hunt, M. L., "Flow-Field Measurements in Supersonic Film Cooling Including the Effect of Shock Wave Interaction," *AIAA Journal* (submitted for publication).

[23]Juhany, K. A., "Supersonic Film Cooling Including the Effect of Shock Wave Interaction," Ph.D. Dissertation, California Inst. of Technology, Pasadena, CA, 1993.

[24]Lappas, A., "An Adaptive Lagrangian Method for Computing 1-D Reacting Flows and the Theory of Riemann Invariant Manifolds for the Compressible Euler Equations," Ph.D. Dissertation, California Inst. of Technology, Pasadena, CA, 1993.

[25]Hefner, J. N., "Effect of Geometry Modification on Effectiveness of Slot Injection in Hypersonic Flow," *AIAA Journal*, Vol. 14, No. 6, 1976, pp. 817, 818.